The Canadian Mineralogist
Vol. 56, pp. 331-354 (2018)
DOI: 10.3749/canmin.1700038

REE REDISTRIBUTION TEXTURES IN ALTERED FLUORAPATITE: SYMPLECTITES, VEINS, AND PHOSPHATE-SILICATE-CARBONATE ASSEMBLAGES FROM THE NOLANS BORE P-REE-Th DEPOSIT, NORTHERN TERRITORY, AUSTRALIA

Michael ANENBURG[§], Antony D. BURNHAM, and John A. MAVROGENES

Research School of Earth Sciences, Australian National University, Canberra ACT 2601, Australia

Abstract

The geochemical behavior and genesis of rare earth element (REE) ores remains poorly understood. In addition, the processes responsible for many features observed in REE ore deposits are not easily determined. Importantly, the distinction between igneous *versus* post-magmatic genesis, or the nature of the mineralizing and modifying fluids or melts, remains in dispute. Nolans Bore is a P-REE-Th deposit in the Northern Territory, Australia, hosting REE mineralization in fluorapatite and its alteration products. These mineralization textures are imaged in 3D by X-ray computed tomography and in 2D by electron microscopy, cathodoluminescence, and X-ray mapping. Primary igneous REE-rich fluorapatite was replaced in two stages. The first, at high temperature, was to endmember fluorapatite-britholite symplectite. The second, at lower temperatures, was to hydrothermal veins and patches comprised of REE-Th phosphate, silicate, and carbonate minerals. Quadrivalent Ce occurs together with Th, suggesting oxidized, low-temperature conditions. Strikingly similar textures are observed at Hoidas Lake, Saskatchewan, Canada, where igneous immiscibility or a pegmatitic boundary layer have been implicated in their formation. Our textural and chemical investigations establish that these symplectites and other similar textures are not primary igneous textures, but formed by subsequent cooling and alteration. Understanding the processes that formed these symplectic and vein textures is key to their theoretical and experimental modeling and should lead to a better understanding of "hydrothermal" REE deposits globally. The decoupling of Ce from the rest of the REE and the mineralogical preferences of the light REE *versus* the heavy REE should be considered when evaluating similar ore deposits for their economic value and mineral processing.

Keywords: fluorapatite, carbonatite, cerium anomaly, phosphate, REE-carbonates, critical metals, thorite, stetindite, rhabdophane.

Introduction

Rare earth elements (REE: La to Lu), a group of technologically critical metals (Hoatson *et al*. 2011, Atwood 2012, Chakhmouradian & Wall 2012, Linnen *et al*. 2014, Wall 2014), are mostly obtained from carbonatites or carbonatite-related ore deposits (Chakhmouradian & Zaitsev 2012, Verplanck *et al*. 2016). REE-rich carbonatites are commonly hydrothermally altered and overprinted, such that some degree of REE mobility is observed. REE can be redistributed *in situ* into different minerals (commonly LREE; Andrade *et al*. 1999, Ruberti *et al*. 2008, Doroshkevich *et al*. 2009, Cooper *et al*. 2015, Moore *et al*. 2015, Trofanenko *et al*. 2016, Andersen *et al*. 2017), or transported externally from the carbonatite to a secondary distal deposit (commonly HREE; Bühn 2008, Andersen *et al*. 2016, Bodeving *et al*. 2017, Broom-Fendley *et al*. 2017a, b). The REE are also considered hydrothermally mobile based on theoretical and experimental studies (*e.g*., Williams-Jones *et al*. 2012, Migdisov & Williams-Jones 2014, Migdisov *et al*. 2016). However, these theoretical and experimental studies represent simplified model systems that might miss geochemical complexities of natural systems. Fluorapatite is a typical mineral in carbonatites and commonly hosts significant amounts of REE (Chakhmouradian *et al*. 2017). Alteration of apatite releases crystal-bound REE into hydrothermal systems, making them available for transport by aqueous fluids. It is thus crucial to document the secondary alteration textures and qualitative geochemical signa-

§ *Corresponding author e-mail address*: michael.anenburg@anu.edu.au

tures of igneous REE-rich fluorapatite to better understand the fate of REE in such hydrothermal systems. The mineral assemblage and composition of the secondary alteration can reveal whether the REE were redistributed or recrystallized *in situ*, leached and possibly deposited elsewhere, enriched or depleted by supergene processes, *etc*. Also, studies of secondary alteration chemistry can reveal differential mobilities of REE (*e.g*., LREE *versus* HREE). It is thus important to distinguish and recognize secondary alteration from primary mineralization, which may not be obvious.

Nolans Bore is a Mesoproterozoic P-REE-Th-U ore deposit in the Northern Territory, Australia, which is composed of centimeter- to meter-wide veins and dikes of fluorapatite. The Nolans project is being developed by Arafura Resources for production of REE and P. It was thought to have formed from phosphate-rich hydrothermal fluids or from evolved carbonatitic or alkali associated melts, but no cognate source has been identified (Huston *et al*. 2016). Instead, it has recently been reconsidered as an igneous cumulate that crystallized directly from carbonatitic melt (Anenburg & Mavrogenes 2018). In this scenario, Nolans Bore was initially composed of REE-rich fluorapatite (*via* britholite substitution: $Ca^{2+} + P^{5+} \leftrightarrow REE^{3+} + Si^{4+}$), which experienced several episodes of hydrothermal alteration (Schoneveld *et al*. 2015, Huston *et al*. 2016). This alteration transformed the fluorapatite to REE-poor fluorapatite with abundant inclusions and veins of REE and Th phosphate, silicate, and carbonate minerals. The alteration mostly redistributed REE and Th between minerals within Nolans Bore itself, and did not transport any of these elements into the wall rocks (Schoneveld *et al*. 2015).

Here we document the textures that resulted from alteration of an initially REE-rich fluorapatite at Nolans Bore. We also compare it to Hoidas Lake, a similar ore deposit in Saskatchewan, Canada, which contains nearly identical textures (Pandur *et al*. 2015, 2016).

Methods

Scanning electron imaging was conducted using a Hitachi S-4300 SE/N field emission-scanning electron microscope (FE-SEM) at the Centre for Advanced Microscopy, Australian National University (ANU). A Gatan MonoCL4 Elite cathodoluminescence (CL) system installed on an FEI Verios FE-SEM was used to generate color-CL images from three composite images acquired using red (620–750 nm), green (525–555 nm), and blue (390–485 nm) Edmund Optics filters.

X-ray element mapping was conducted using WDS (wavelength dispersive spectroscopy) *via* a Cameca SX100 electron probe microanalyzer (EPMA) at the Research School of Earth Sciences (RSES), ANU. Beam conditions for the EPMA were 15 kV accelerating voltage, 100 nA beam current, and a spot size of 1 μm. Mapping resolution was 256 by 192 pixels, with a pixel dwell time of 150 ms and 1 μm step size. A list of analyzed elements and their X-ray lines are given in Table 1. The raw count data were then plotted as matrices and phase maps using hexagonal binning, with hexagon greyscale intensities corresponding to the log-transform of the counts for that bin. Coordinates of raw data for each map were corrected for beam drift between subsequent passes, as only four elements could be analyzed simultaneously. Therefore, scatter plots of elements measured in different passes have more noise relative to those measured in a single pass. Ratios and absolute values of La and Ce counts (see La-Ce cell in the matrix) were used to construct the phase map. For details of the procedure and source code written in R, see the supplementary information (available from the Depository of Unpublished Data on the MAC website, document REE Redistribution Textures CM56_10.3749/canmin.1700038).

TABLE 1. X-RAY EMISSION LINES AND WDS CRYSTALS USED FOR MAPPING, FOLLOWING THE GUIDELINES OF PYLE *et al.* (2002)

Element	Line	Crystal
Si	$K\alpha_1$	TAP
P	$K\alpha_1$	PET
Ca	$K\alpha_1$	PET
Fe	$K\alpha_1$	LIF
Y	$L\alpha_1$	TAP
La	$L\alpha_1$	LIF
Ce	$L\alpha_1$	LIF
Pr	$L\beta_1$	LIF
Nd	$L\beta_1$	LIF
Sm	$L\beta_1$	LIF
Th	$M\alpha_1$	PET

Three-dimensional X-ray micro computed tomography (XRCT) was conducted using a HeliScan MicroCT system at the X-ray Micro Computed Tomography lab (CTLab) at ANU to yield images at a resolution of approximately 2 μm (Latham *et al*. 2008, Myers *et al*. 2011, Varslot *et al*. 2011). A polychromatic X-ray beam with an energy of 120 kV and tube current of 50 μA was used. XRCT data for the sample was rendered using Drishti v2.3.2 (Limaye 2012). X-ray absorption scales with density and atomic number, and therefore a backscattered electron image (Fig. 1) is approximately equivalent to an XRCT image, such as Figure 2.

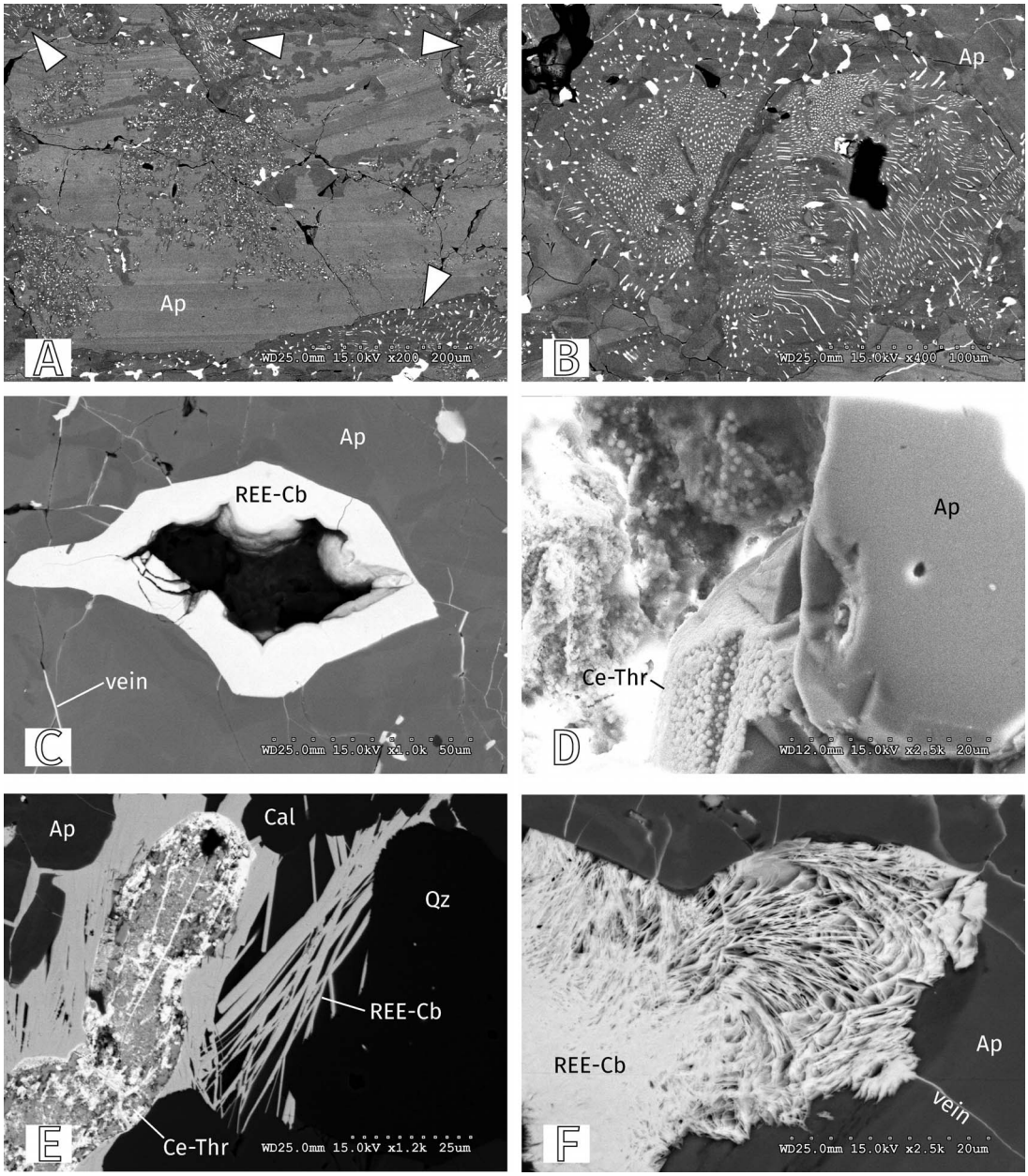

FIG. 1. Scanning electron images showing secondary alteration textures in fluorapatite from Nolans Bore. (A) Sample 153-35B: Coarse primary REE-rich fluorapatite with a horizontal fine oscillatory zoning pattern (medium grey) altered to REE-poor fluorapatite (dark grey) and REE-rich phases (white). Arrows denote symplectic alteration zones. (B) Sample 153-35B: Close-up of a symplectic alteration zone. (C) Sample 291-10A: Fluorapatite-hosted pore with REE-rich phases coating the interior walls. (D) Sample 157-4C: Close up of a boytroidal aggregate composed of nanometer-scale REE- and Th-rich minerals. (E) Sample 157-4C: An unknown bladed REE-carbonate mineral and an aggregate of REE-Th silicate and phosphate minerals. (F) Sample 157-4C: Fibrous carbonate, most likely calcioancylite-(Nd), in fluorapatite. Note growth at the vein–pore interface.

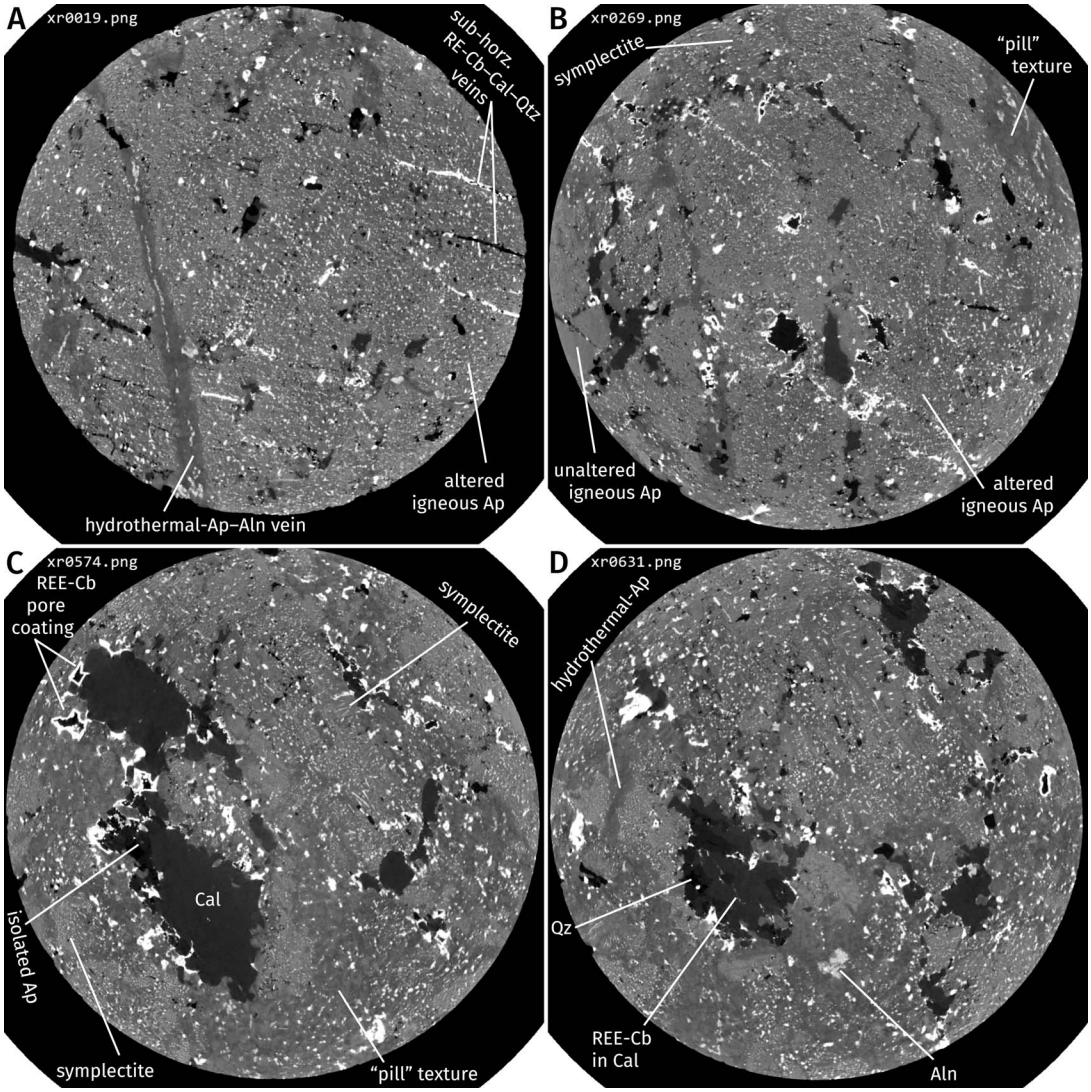

FIG. 2. (A–H) Extracted still frames from a cylindrical bottom-to-top basal section XRCT scan of sample 153-35, 7.5 mm long and 4.0 mm wide, available in Supplementary Video 1. Brightness increases from pores (black) → talc, humite-group minerals, quartz → calcite → REE-poor fluorapatite → REE-rich fluorapatite → allanite → REE and Th-rich phases (white). Frame number is given in the top left corner of each panel.

Trace elements were acquired using laser ablation-inductively coupled plasma-mass spectrometry (LA-ICP-MS) *via* an Agilent 7700 quadrupole mass spectrometer coupled to a Coherent CompexPro 193 nm ArF excimer laser using methods outlined by Eggins *et al*. (1998). NIST-610 was used as a primary calibration standard and BCR-2G as a secondary standard. Ablation time was 20 s on background (laser off) and 40–45 s of sample measurement (laser on). Data were reduced using Iolite 2.5 running on Igor Pro 6.37 (Woodhead *et al*. 2007, Paton *et al*. 2011). Full analytical details and results are freely available on Figshare at https://doi.org/10.6084/m9.figshare.5602720 or by request from the corresponding author.

GEOLOGICAL SETTING

The geological history of Nolans Bore has been described by Schoneveld *et al*. (2015) and Huston *et al*. (2016) and of the Aileron province, more

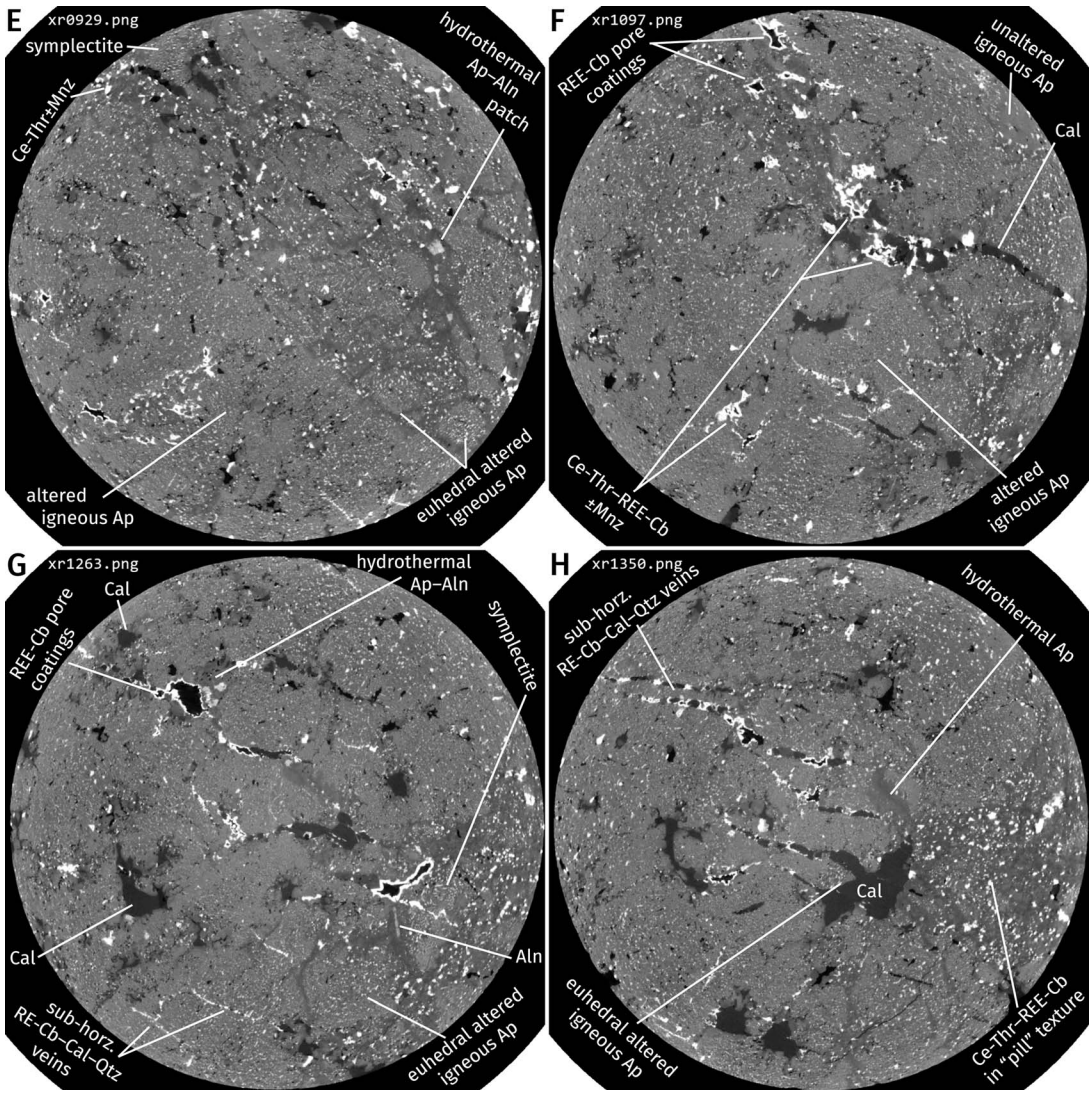

FIG. 2. (continued)

generally, by Scrimgeour (2013). Therefore, only a summary relevant to this work is given here. The Nolans Bore fluorapatite-diopside-hyalophane veins formed at *ca*. 1525 Ma in shear zones within granulite-facies gneisses and schists (Huston *et al*. 2016) during the late stages of the Chewings Orogeny (Dirks *et al*. 1991, Vry *et al*. 1996, Claoué-Long *et al*. 2008, Anderson *et al*. 2013). Peak conditions were estimated to have been *ca*. 850 °C and 7 kbar (Morrissey *et al*. 2014). The Nolans Bore mineral assemblage is consistent with formation by reaction of a moderately magnesian carbonatite with the silicate wall rocks at 750–850 °C (Anenburg & Mavrogenes 2018). Nolans Bore was subsequently affected by two metamorphic events: (1) the Redbank Thrust Zone event at 1500–1400 Ma (Shaw & Black 1991) and (2) the Alice Springs Orogeny at 450–300 Ma (Haines *et al*. 2001, Buick *et al*. 2008). These events resulted in regional shearing, hydrothermal activity, and metasomatism (Shaw & Black 1991, Hand & Sandiford 1999, Raimondo *et al*. 2011). Peak conditions for the Alice Springs Orogeny are estimated to have been *ca*. 550 °C and 5 kbar (Raimondo *et al*. 2012). These regional metamorphic events also affected Nolans Bore, resulting in the REE redistribution textures discussed in this article.

An additional thermal event at *ca*. 1140 Ma may also have overprinted the primary igneous features at Nolans Bore (the Teapot event; Shaw & Black 1991, Biermeier *et al*. 2003).

Petrography

Nolans Bore is composed primarily of fluorapatite and its alteration products. We highly recommend that the reader view Supplementary Video 1 alongside this section for a better understanding of the three-dimensional textures discussed. Idealized compositions of the mineral phases are given in Table 2. Four different types of fluorapatite are present, distinguished by their compositions and textures:

Primary igneous fluorapatite. This type of fluorapatite is characterized by millimeter- to centimeter-scale euhedral to subhedral crystals with common oscillatory growth zones (Figs. 1A, 2B). This fluorapatite appears dull-green in SEM-CL (Fig. 3A) and is composed of strong narrow peaks at about 600 and 630 nm and a weaker, wider peak at 450 nm (Fig. 3C). Although primary fluorapatite should be yellow or bright green in the images (given the strong 600 nm peak), it is not (in this case) because the RGB filters used in the CL system do not transmit yellow light. Patches of finer-grained rounded fluorapatite aggregates (termed pill texture by Chakhmouradian *et al*. 2017) are also observed (Fig. 2B, H). The igneous fluorapatite contains *ca*. 5% total rare earth element oxides with a smooth LREE-enriched pattern (Schoneveld *et al*. 2015). Its REE-rich nature is evident by its brightness observed in BSE and XRCT images. The morphology of this fluorapatite is consistent with types 1 and 2 of Chakhmouradian *et al*. (2017), interpreted by them to crystallize from the carbonatitic magma (also observed by Decrée *et al*. 2016).

Primary hydrothermal fluorapatite. This is commonly found between grains of igneous fluorapatite (as mesostasis), protruding into cavities, or as rare veins (Fig. 2A, D, E, G, H). It is commonly associated with allanite and rare ekanite. It is poorer in LREE than igneous fluorapatite due to its co-crystallization with allanite. Therefore, it appears darker in BSE and XRCT images.

Symplectic fluorapatite. Symplectic fluorapatite consists of a micrometer-scale vermicular britholite-group mineral hosted by fluorapatite (Figs. 1A, B, 2B, C, E). It appears as euhedral to subhedral alteration domains within igneous fluorapatite, with the BSE and XRCT brightness of the fluorapatite matrix matching that of the REE-rich adjacent unaltered primary fluorapatite. Supplementary video 2 and Figure 4 show the three-dimensional shape of one symplectite region.

TABLE 2. MINERAL NAMES AND ENDMEMBER FORMULAE

Mineral	Formula
Silicates	
Thorite	$ThSiO_4$
Stetindite	$CeSiO_4$
Allanite	$Ca(REE,Th)Al_2Fe(SiO_4)_3(OH)$
Britholite	$(REE,Th)_3Ca_2(SiO_4)_3(F,OH)$
Calciothorite	$(Th,Ca_2)SiO_4{\cdot}3.5H_2O$
Thorogummite	$Th(SiO_4)_{1-x}(OH)_{4x}$
Coffinite	$U(SiO_4)_{1-x}(OH)_{4x}$
Soddyite	$(UO_2)_2SiO_4{\cdot}2H_2O$
Ekanite	$Ca_2ThSi_8O_{20}$
Phosphates	
Apatite	$Ca_5(PO_4)_3(F,OH)$
Monazite	$REEPO_4$
Rhabdophane	$REEPO_4{\cdot}H_2O$
Carbonates	
Bastnäsite	$REECO_3F$
Parisite	$CaREE_2(CO_3)_3F_2$
Synchysite	$CaREE(CO_3)_2F$
Ancylite	$REESr(CO_3)_2(OH){\cdot}H_2O$
Calcioancylite	$REECa(CO_3)_2(OH){\cdot}H_2O$
Galgenbergite	$CaREE_2(CO_3)_4{\cdot}H_2O$
Oxides	
Thorianite	ThO_2

Secondary altered fluorapatite. This type of fluorapatite is characterized by alteration of primary fluorapatite into REE-poor fluorapatite with abundant inclusions of REE and Th-rich phases, connected by a mesh texture of thin (0.5 to 2 μm) veins composed of the same phases (Figs. 1A, C–F, 2). The altered fluorapatite is REE-poor, appears dark in BSE and XRCT images, and appears bright blue to violet in SEM-CL (Fig. 2B). In contrast to igneous fluorapatite, altered fluorapatite has weaker peaks at 600 and 630 nm and the lower wavelength peak is shifted slightly towards 400 nm. The morphology of this fluorapatite is consistent with the hydrothermally altered type 3 fluorapatite discussed by Chakhmouradian *et al*. (2017). Our secondary fluorapatite is also texturally similar to altered fluorapatites from carbonatites (*e.g*., Narasayya & Sriramadas 1974, Nadeau *et al*. 2015, Feng *et al*. 2016, Prokopyev *et al*. 2017) and elsewhere (Pan *et al*. 1993, Li & Zhou 2015, Uher *et al*. 2015, Jonsson *et al*. 2016, Ondrejka *et al*. 2016, Zeng *et al*. 2016, Lupulescu *et al*. 2017). The two most common fluorapatite alteration products are REE-carbonates and Ce-Th-silicates. The REE-carbonates consist of parisite, galgenbergite, and calcioancylite (Schoneveld *et al*. 2015, Huston *et al*. 2016), with the dominant REE in each of these being La, Ce, or Nd, varying

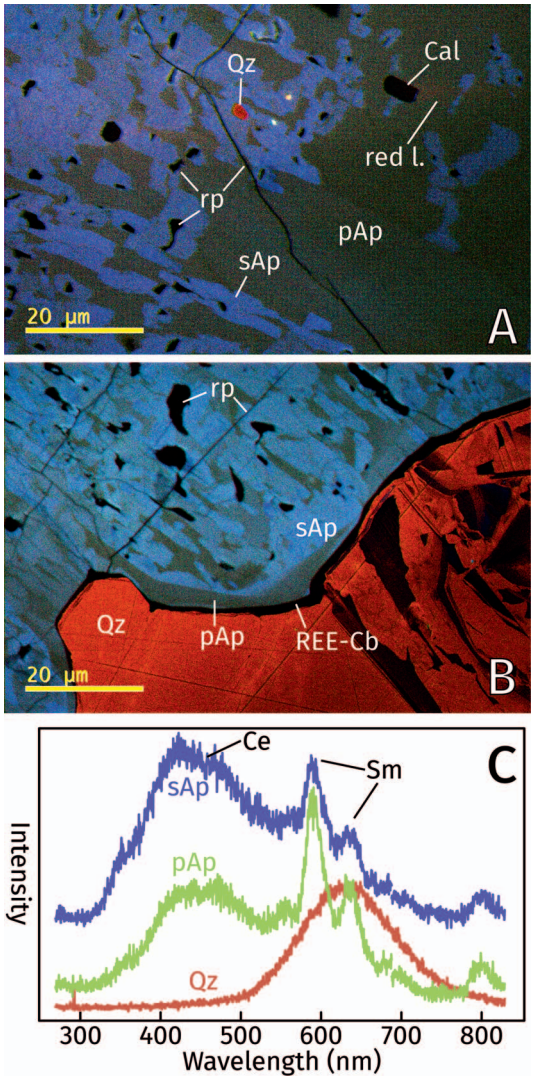

FIG. 3. (A, B) Cathodoluminescence RGB composite images of selected areas of sample 157-5A. Calcite does not luminesce immediately when hit by the electron beam, and its luminescence lifetime exceeds the dwell time of the electron beam. Therefore, it appears black with a faint streak of red luminescence (red l.) to its right (*i.e.*, in the beam scanning direction). (C) Cathodoluminescence spectra of secondary fluorapatite (purple), primary fluorapatite (green), and quartz (red). Different spectra are not to scale, and the intensity is in arbitrary units. The sharp peaks at *ca*. 600 and 630 nm most likely correspond to Sm^{3+}, and the wide peak at 450 nm corresponds to Ce^{3+} (Waychunas 2002, Gros *et al*. 2016). Abbreviations: pAp – primary fluorapatite; sAp – secondary fluorapatite; rp – REE-phase.

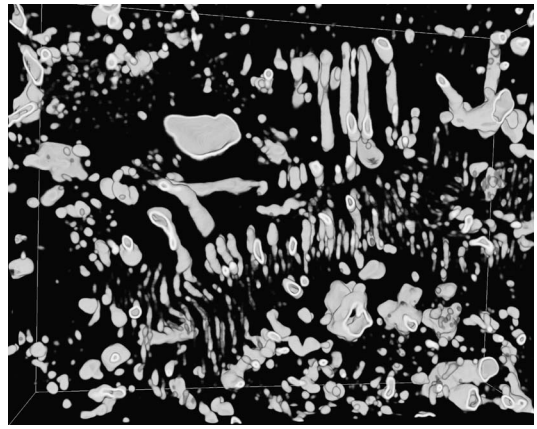

FIG. 4. A still frame from Supplementary Video 2 showing the three-dimensional shape and distribution of symplectic britholite and other REE-Th-rich phases within the matrix fluorapatite. The video sweeps through a 10 µm thick section. The width of the section is *ca*. 30 µm.

across growth zones in the same crystal (*e.g.*, Schoneveld *et al*. 2015). The REE-carbonates are commonly boytroidal coatings on the walls of pores, exhibiting an irregular ring-shaped morphology in polished section (Fig. 1C, D). In other cases, they are euhedral, and often bladed (Fig. 1E). Calcioancylite-(Nd) occasionally appears as curved fibers or plates (Fig. 1F). The Th-Ce silicates include thorite, stetindite, and intermediate solid solutions, with several compositions present in the same vein or pore (Fig. 1E). Other less-common alteration phases include monazite, allanite, and thorianite (Schoneveld *et al*. 2015, Huston *et al*. 2016). The multiphase, hydrated, porous, and metamict nature of these phases commonly results in mixed analyses and low analytical totals when analyzed by EDS, suggesting the phases may in fact be—at least partially—rhabdophane (hydrated REE phosphate) instead of monazite, calciothorite, "thorogummite" (metamict and hydrated Th silicates), and hydrated REE carbonates such as hydroxylparisite. Some of the larger veins, occasionally up to several millimeters thick, are composed mostly of calcite, with minor REE-carbonates (occasionally present along calcite cleavage planes, Fig. 2D), hydrous Mg-silicates (talc or humite-group minerals), and quartz.

Nolans Bore is dominated by secondary altered fluorapatite. The distribution of the relict igneous fluorapatite seems random and does not correlate with depth or location within the deposit, other than being completely absent in the shallow supergene zones (Schoneveld *et al*. 2015). The degree of alteration seems to correlate with the initial REE content of the

TABLE 3. AVERAGES OF MINERAL COMPOSITIONS MEASURED BY EDS, GIVEN IN wt.%

	Fluorapatite symplectite	Fluorapatite igneous	Fluorapatite altered	Stetindite	Thorite
n	4	8	7	2	3
SiO_2	4.03	2.64	2.64	26.33	28.24
Al_2O_3	bdl	bdl	0.09	0.91	0.55
MgO	bdl	bdl	0.37	bdl	0.49
CaO	47.11	49.99	49.02	2.16	2.98
SrO	0.77	0.86	1.11	bdl	bdl
La_2O_3	1.44	0.78	0.70	bdl	bdl
$Ce_2O_3^{(T)}$	4.50	2.37	2.73	42.19	1.23
Nd_2O_3	1.82	1.08	1.05	4.76	7.37
ThO_2	1.09	0.29	0.34	3.57	40.88
P_2O_5	34.39	37.13	37.91	bdl	bdl
SO_3	0.74	0.76	0.33	bdl	bdl
F	2.91	3.15	3.16	bdl	bdl
Cl	0.02	0.03	bdl	bdl	bdl
Total	98.81	99.06	99.44	79.91	81.74

bdl: below detection limit, *n*: number of analyses.

fluorapatite, resulting in less-intense alteration of the hydrothermal primary fluorapatite. Likewise, igneous pill-textured fluorapatites are preferentially preserved due to lower REE contents relative to the coarser fluorapatites. Symplectic fluorapatite is extremely rare. The focus of this work is the transformation of primary igneous to symplectic and secondary fluorapatite. The formation of Nolans Bore and the primary fluorapatite will be discussed in a future publication.

Mineral Chemistry

Due to the small size of the alteration products, it was not possible to obtain meaningful compositions of each individual phase, and semi-quantitative compositions obtained by EDS are given in Table 3. Instead, we used two methods: qualitative major and minor element mapping by EPMA and trace element characterization of alteration regions by LA-ICP-MS.

EPMA mapping

Element correlation plots, derived from element maps, are shown in Figure 5. Additionally, a phase map using La-Ce abundance ratios was drawn to emphasize the textural association of each phase. The maps were measured with 1 μm steps, but the analyzed volume is larger due to electron scattering and secondary fluorescence (Reed 2006). Because the REE-rich phases are on the scale of sub-μm to a few μm, the arrays in the matrix show mixing lines between the most volumetrically dominant fluorapatite and the other less-abundant endmembers present in each field of view. Yttrium is used as a proxy for the HREE, which are below detection by EPMA. Figure 5A shows a symplectite-dominated field of view from sample 153-35B. Using the La-Ce plot, at least four distinct phases can be clearly distinguished and can also be seen in most of the other matrix cells. The most common phase is REE-poor fluorapatite (light green), clearly seen on the WDS maps, phase map, and matrix as the P-rich phase poor in all other elements. A second phase (dark green) appears to contain both LREE and HREE. This phase forms the REE-rich part of the symplectite. We suggest that this phase is britholite or fluorcalciobritholite (see Pekov *et al*. 2007 for the distinction between the two). A third phase (pink) contains Th and Ce, is Si-rich, and shows a preference for HREE, with some Nd and virtually no La. We interpret this phase to be a thorite–stetindite solid solution. The last phase (purple) is an LREE phase with exceptionally high La contents, some P and Si, but no Th and Ce. We are not aware of any mineral that qualitatively fits this composition and suspect it is a new, unknown mineral. Possibly, it is the britholite-cerite-like mineral reported by Holtstam & Andersson (2007) and synthesized in the hydrothermal experiments of Anenburg & Mavrogenes (2018). Even though some phases seem to be part of the symplectite, their composition is different from britholite. Only the thin elongated phases (*e.g.*, top right of the maps) are britholite—thus forming part of the symplectite—whereas the similar looking but slightly larger rounded phases (*e.g.*, bottom center), which lack REE other than Ce, are thorite–stetindite. Figure 5B shows a vein-dominated field of view from sample 157-5A. REE-poor fluorapatite is again the dominant phase (here in light cyan). Relict unaltered primary fluorapatite,

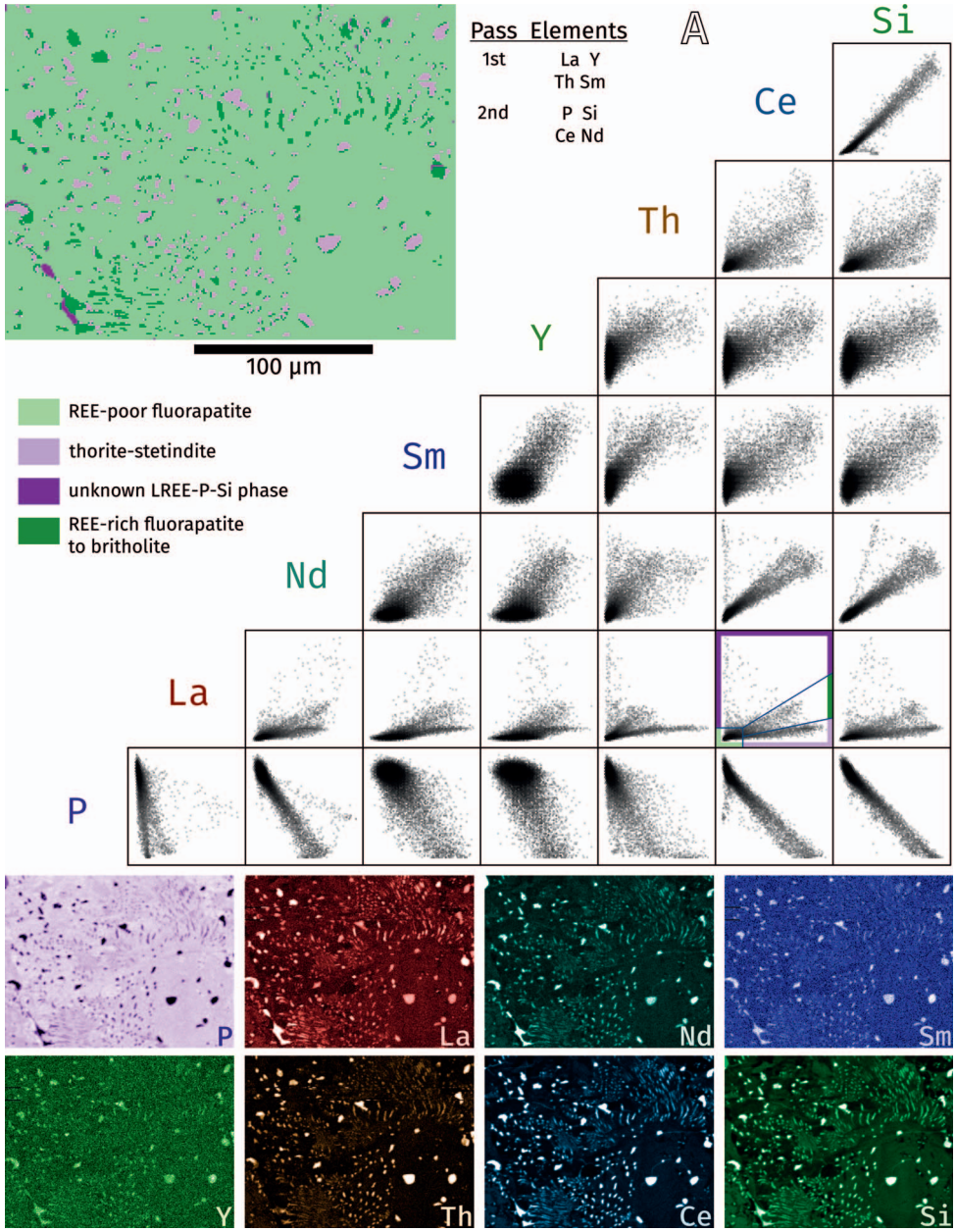

FIG. 5. Qualitative scatter-plot matrix of counts obtained by WDS mapping for various elements (middle), individual WDS maps (bottom), and a phase map (top left). Most scatter plots show three mixing lines, implying four components. The discriminant functions used to distinguish the four phases are shown in colors corresponding to the phase maps on the La *versus* Ce scatter plot. (A) Sample 153-35B.

equally rich in all REE and Th, is light brown. The same color represents rare patches of REE-rich phospho-silicate, most likely britholite. A third phase (dark brown) is similar to the Ce-Th-silicates mentioned above, and here it occurs in veins in addition to the patches observed in sample 153-35B. The dark cyan veins are interpreted as two separate phases, *i.e.*, the unknown LREE-P-Si phase described above and an

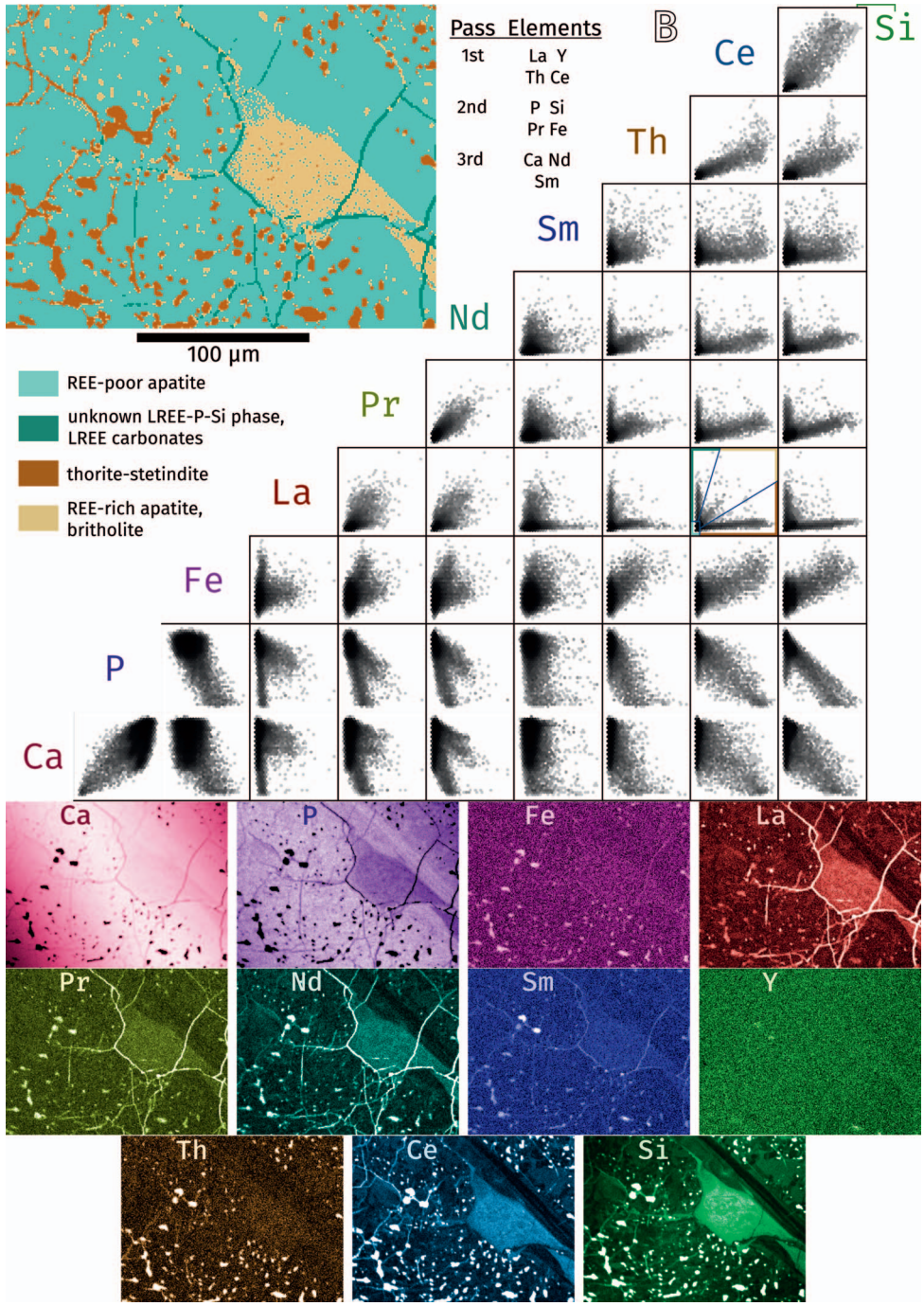

FIG. 5. (continued) (B) Sample 157-5A.

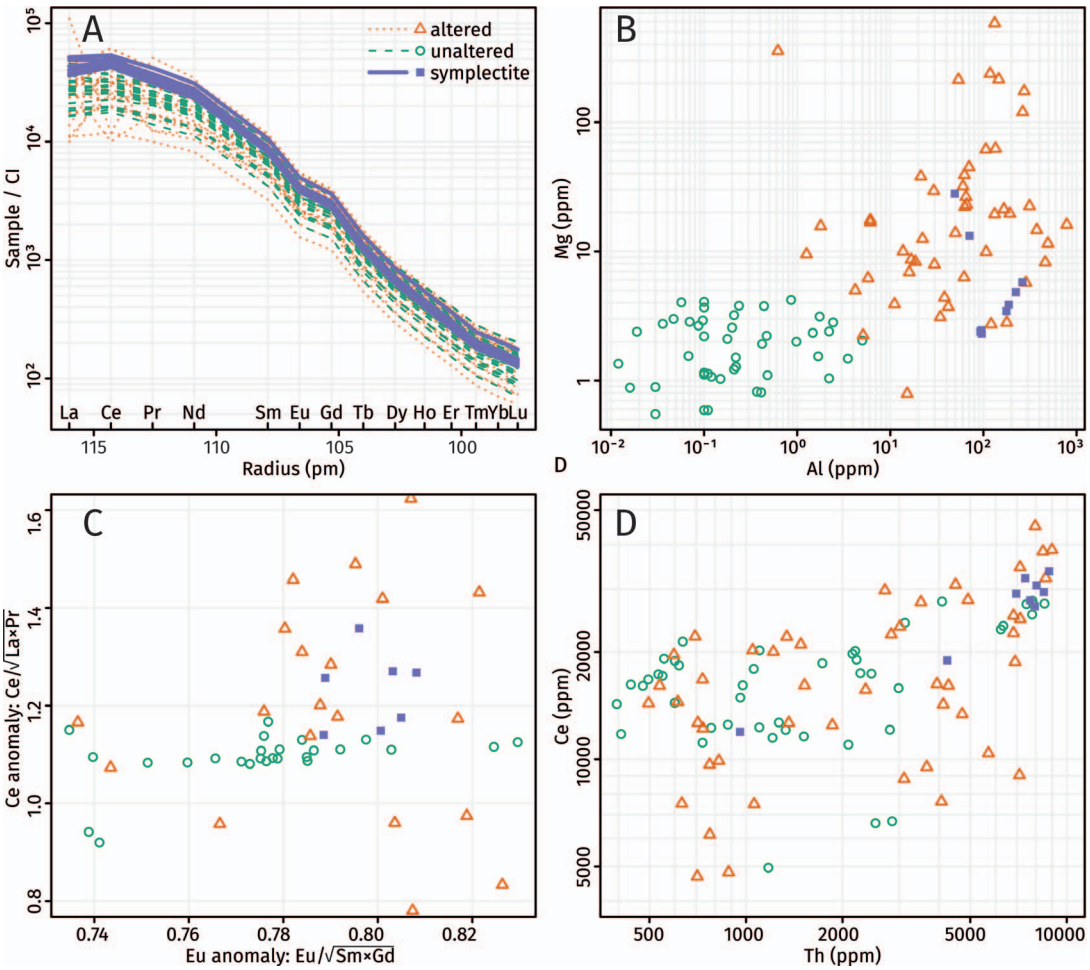

FIG. 6. Rare earth and trace elements in fluorapatite analyzed by LA-ICP-MS. Unaltered analyses are of pure fluorapatite. Altered and symplectite analyses are of fluorapatite and inclusions. (A) REE patterns with normalization values from O'Neill (2016). (B) Mg *versus* Al. (C) Ce *versus* Eu anomalies. The higher-than-unity value $(\mathrm{Ce}/\sqrt{(\mathrm{La}\times\mathrm{Pr})} \approx 1.1)$ is an artifact of interpolating through curvature and does not signify a positive Ce anomaly. (D) Ce *versus* Th.

LREE carbonate, with low P and Si in most points. The carbonate interpretation is also supported by the occurrence of REE-carbonates where the veins intersect pores (*e.g.*, Fig. 1F).

REE patterns and trace element compositions

The rare earth element patterns presented here are similar to the results obtained by Schoneveld *et al.* (2015) and Huston *et al.* (2016), with a steep LREE-enriched slope ($La_N/Lu_N \approx 500$) and flattening in the lightest LREE (Fig. 6A). As observed in Table 3, the symplectites are the REE-richest domains and hydrothermal alteration mostly affects the LREE and the Ce anomaly (Fig. 6A). The addition of Mg and Al hinted at by the EDS analyses (Table 3) is clear in the LA-ICP-MS data, with a clear distinction between unaltered primary fluorapatite and hydrothermally altered fluorapatite (Fig. 6B). Symplectic fluorapatite plots well within the hydrothermally altered field. All fluorapatite analyses show a moderately negative Eu anomaly with a restricted range of 0.74–0.82. Symplectic fluorapatite analyses show a narrower range of 0.79–0.81, but are not significantly different from either the altered or unaltered fluorapatites. There is no Ce anomaly for the primary fluorapatite grains (Fig. 6C). On the other hand, hydrothermally altered fluorapatites show a variety of Ce anomalies (likely determined by the inclusion or lack of thorite or

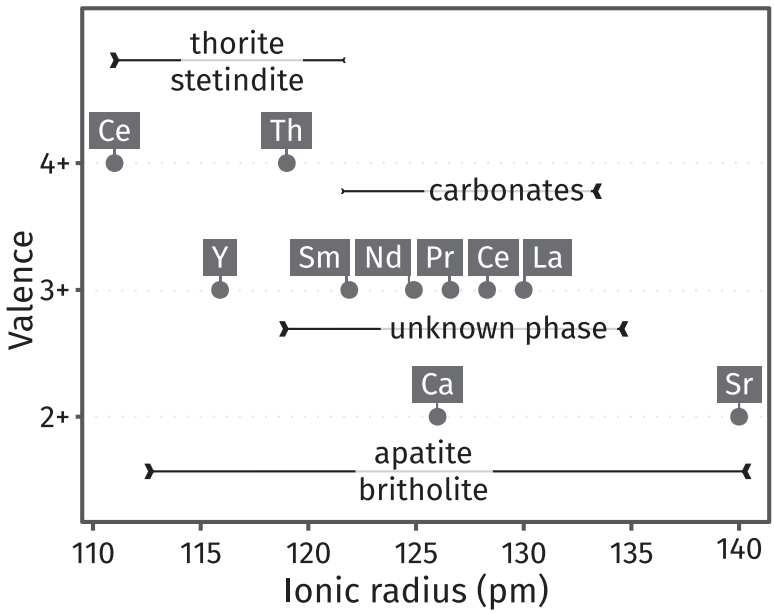

FIG. 7. Ionic radii *versus* valence of elements appearing in mineral phases appropriate to this study, with approximate element preference for each mineral phase. The arrowhead size represents the degree of preference a phase has for cations of that radius.

stetindite inclusions in the analysis), whereas symplectic fluorapatites show a small positive Ce anomaly (Fig. 6A, C). This anomaly may be caused by loss of non-Ce LREE, rather than by addition of Ce (see discussion below).

DISCUSSION

Hydrothermally altered fluorapatite and the oxidation state of cerium

The REE-bearing phase assemblage that forms during metasomatically induced alteration of fluorapatite (*i.e.*, REE-carbonates and Ce-Th-silicates) is distinct from the symplectites (*i.e.*, britholite). It occurs in veins and pore fillings that form by reduction in molar volume as the fluorapatite loses REE (Oberti *et al*. 2001). Also, La and Ce are decoupled in most of these phases. As La^{3+} and Ce^{3+} behave almost geochemically identically, the absence of Ce from La-rich phases and *vice versa* requires Ce to exist in the quadrivalent instead of the more common trivalent state. This is supported by the occurrence of Ce in Th-rich phases (*e.g.*, thorite–stetindite), as Ce^{4+} behaves in a similar way to Th^{4+}. Figure 7 shows the ionic radii of all elements in discussion for eightfold coordination. It demonstrates the preference in element uptake of each phase: small cations such as Ce^{4+}, Th, Y, and HREE are hosted by silicates in thorite–stetindite solid solutions (as observed by Cooper *et al*. 2015), and larger cations such as LREE (excluding Ce^{4+}) are hosted by carbonates and phosphates with variable silica contents.

The presence of a Ce^{4+}-rich silicate mineral suggests either high oxygen fugacities (fO_2) or low temperatures during the hydrothermal alteration. Although Ce^{3+} stability persists into oxidizing conditions at low pH, this is not the case for Nolans Bore. Acidic conditions would cause breakdown of allanite to hydrous Fe-oxides and aluminosilicates (Meintzer & Mitchell 1988, Berger *et al*. 2008), but the allanite at Nolans Bore is unaltered. The concentration of Ce in zircon (a member of the same mineral group as thorite and stetindite; Förster 2006) is widely recognized as an oxybarometer (Trail *et al*. 2011, Burnham & Berry 2012, Smythe & Brenan 2016), but no zircon formed during hydothermal alteration at Nolans Bore. Trace-element data for coexisting thorite and zircon (Pettke *et al*. 2005) can be used to estimate the composition of a hypothetical zircon that would be in equilibrium with the thorite solid-solution observed at Nolans Bore (see supplementary appendix). Onuma-type parabolic fits (Onuma *et al*. 1968, Blundy & Wood 2003) to the REE (for $D_{Ce^{3+}}$) and to Hf, U, and Th (for $D_{Ce^{4+}}$) in magmatic zircon and thorite from their sample "Yankee 8.1 E" allow us to predict that $D_{Ce^{4+}}/D_{Ce^{3+}}$ is *ca*. 190,000 for zircon and

ca. 1200 for thorite. Hence the Ce anomaly (Ce/Ce*, where $Ce* = \sqrt{La \times Pr}$ after normalizing all three elements to chondritic abundances) in zircon would be 150 times larger than Ce/Ce* in coexisting thorite. Although a quantitative analysis of the thorite–stetindite phase was not possible, the X-ray intensity (Fig. 5B) and EDS (Table 3) data suggest it has Ce/Ce* $>$ 10 (and more probably $>$50), which would correspond to Ce/Ce* $>$ 1500 in zircon. Such exceptional values are seldom encountered in zircon. For example, Ce/Ce* exceeded 1000 in one out of 656 samples in one survey of zircon from a range of rock types (Belousova *et al*. 2002) and six out of 188 samples from a series of oxidized porphyry intrusions in which S was thought to occur primarily as sulfate (Ballard *et al*. 2002). Ce/Ce* for zircon increases with decreasing temperature, with increasing fO_2, and with increasing alkali content in the precipitating fluid (Paul & Douglas 1965, Trail *et al*. 2011, Smythe & Brenan 2016). However, as Ce is predominantly incorporated in fluorapatite as Ce^{3+}, mass-balance considerations necessitate a source of oxygen for a Ce^{4+}-rich silicate to precipitate, and hence the presence of an oxidizing fluid is envisaged. By comparison to the data from natural samples containing magmatic zircon (Ballard *et al*. 2002), whose fO_2 is poorly known but likely formed above the sulfide–sulfate transition (Klimm *et al*. 2012, Matjuschkin *et al*. 2016), the fO_2 during thorite–stetindite precipitation was at least two orders of magnitude above FMQ, but likely much higher. Nolans Bore also contains several hundred ppm of U in addition to Th (Huston *et al*. 2016). It would be expected that U would be enriched to notable levels in the REE and Th minerals, but no U was detected. Instead, U is only observed in late veins in the hydrous minerals coffinite and soddyite (Huston *et al*. 2016), suggesting that the U was transported separately and more effectively than Th. This decoupling is only possible if U is hexavalent (Langmuir 1978), providing further evidence for oxidizing conditions. Moreover, Schoneveld *et al*. (2015) reported parisite and calcioancylite with contrasting Ce-bearing and Ce-absent zones, suggesting oxidation-state fluctuation. This was most likely the latest alteration stage, occurring in or near the supergene zone. Similar boytroidal textures, breaking down of REE-rich fluorapatite, and Ce-La decoupling are known elsewhere from supergene zones (Lottermoser 1990, Andersen *et al*. 2017, Xu *et al*. 2017).

Several studies have explored the metasomatic alteration of REE-bearing apatite by fluids. Experimental studies over the past two decades demonstrate that alteration of REE-rich fluorapatite results in inclusions of monazite and xenotime. The inclusions commonly nucleate within the REE-rich fluorapatite, whereas fluorapatite in the immediate area surrounding the inclusions is depleted in REE (Wolf & London 1995, Harlov *et al*. 2002b, Harlov & Förster 2003, Harlov *et al*. 2005). Our secondary REE-rich phases exhibit identical textures (*e.g*., Fig. 1A), but they are not monazite or xenotime. This is probably because of the high activities of Si and CO_2 relative to P, stabilizing phases other than monazite or xenotime. Harlov *et al*. (2007b) showed that in metasomatism experiments containing both REE and Th, $ThSiO_4$ forms a separate phase from monazite. Thorite formed at low temperatures (300 °C) as aggregates of submicrometer grains with a striking resemblance to the boytroidal textures observed in our samples (Fig. 1D). Ce^{4+} and Th^{4+} have similar ionic radii and thorite and stetindite are isostructural, permitting solid solution. The low-temperature stability of Ce^{4+} and the nanoscale morphology of this phase support our hypothesis that these features formed at similarly low temperatures. Huston *et al*. (2016) reported primary fluorapatite-hosted fluid inclusions with homogenization temperatures up to 400 °C. Given the rarity of primary fluorapatite, their lack of distinction between primary and secondary fluorapatite, and the secondary appearance of fluorapatite in their SEM imaging, we attribute their fluid-inclusion data to secondary alteration, which agrees with the temperature estimates suggested above. Hydrous Th-Ce-silicates and REE-carbonates with similar boytroidal, fibrous, or microfracture-filling textures are widely known elsewhere and are always interpreted as having formed *via* hydrothermal Th and REE redistribution at *ca*. 400 °C or lower (*e.g*., Ermolaeva *et al*. 2007, Seydoux-Guillaume *et al*. 2012, Savelyeva *et al*. 2016, Macdonald *et al*. 2017a, Macdonald *et al*. 2017b, Savelyeva *et al*. 2017).

Symplectite formation

Symplectites are vermicular intergrowths of two or more phases considered to form by subsolidus unmixing or replacement processes during cooling, metamorphism, and metasomatism, generally in the presence of limited amounts of fluid (see Gaidies *et al*. 2017, Spruzeniece *et al*. 2017, and references therein). Notable examples are myrmekite (metasomatic replacement of K-feldspar by sodic plagioclase and quartz), kelyphite (decompression-induced breakdown of garnet to anorthite, orthopyroxene, and spinel), muscovite-quartz, amphibole/clinopyroxene-plagioclase, *etc*., particularly from metamorphic rocks where subsolidus reactions dominate. The formation of pearlite (α-Fe and Fe_3C) by slow cooling of carbon steel is another example, from the field of metallurgy.

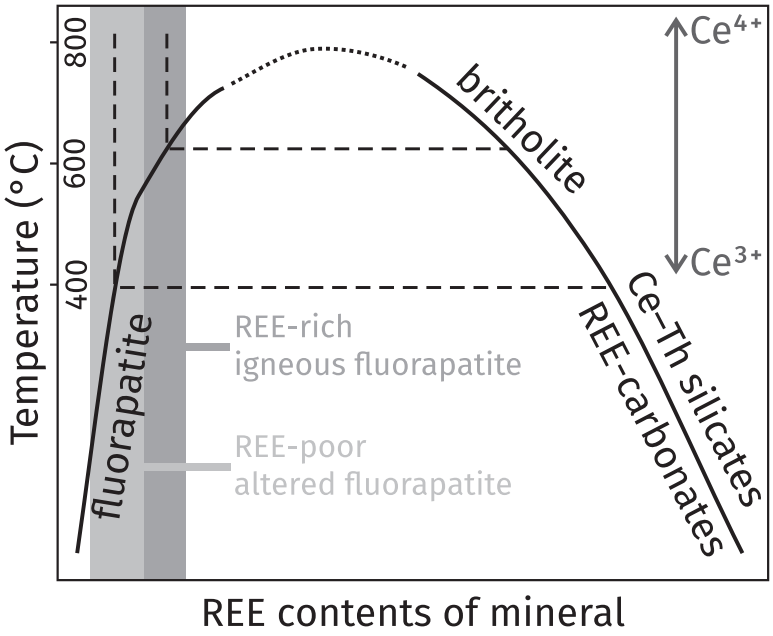

FIG. 8. A schematic phase diagram showing secondary processes in Nolans Bore fluorapatite. Igneous REE-rich fluorapatite is stable at high temperatures above a solvus. As the system cools, a solvus is encountered, causing exsolution of britholite from fluorapatite as symplectites. Further cooling reduces the amount of REE soluble in fluorapatite and oxidation of Ce^{3+} to Ce^{4+}. The high CO_2 and Si activities stabilize carbonate and silicate minerals instead of phosphates as fluorapatite alteration phases.

Primary fluorapatite contains REE and Y as well as Th as an intermediate fluorapatite–britholite solid solution. Figure 5A shows perfect mixing lines between REE-poor fluorapatite, REE-rich fluorapatite, and britholite. This suggests that the apatite–britholite symplectites formed during isochemical subsolidus exsolution (with respect to major elements), most likely along a solvus during slow cooling. Both LREE and HREE are present in the fluorapatite and britholite, as expected from the relatively flat partition coefficient pattern for the REE in carbonatitic fluorapatites (Brassinnes *et al*. 2005, Hammouda *et al*. 2010, Chakhmouradian *et al*. 2017).

The symplectites most likely formed at temperatures higher than the hydrothermally altered fluorapatite. Fluorapatite and britholite exhibit complete miscibility at high temperatures (Boyer 1997), but form two phases along a solvus at lower temperatures (Fig. 8; Anenburg & Mavrogenes 2018). This miscibility gap is poorly characterized, but there are plenty of hints as to its existence. For example, Betkowski *et al*. (2016) reported coexisting fluorapatite and britholite at 500 and 600 °C and 1 kbar. The CaO contents of the britholite increased from ~8.3 to ~13.8% with temperature, indicating a higher fluorapatite component in britholite. Similarly, Budzyń *et al*. (2017) reported increasing REE contents from ~30 to 40% in fluorapatite with increasing temperature from 450 to 750 °C. Anenburg & Mavrogenes (2018) showed that an appreciable solid solution between fluorapatite and britholite is only observed at 700 °C and above, and two immiscible phases occur at lower temperatures. Additionally, Budzyń *et al*. (2011) synthesized coexisting fluorapatite and britholite at 450 and 500 °C. Symplectites in similar systems were reported by Betkowski *et al*. (2016) to occur at 600 °C, but were absent at 500 °C. Observations from natural rocks confirm the apatite–britholite miscibility gap forming during late stages of igneous activity below *ca*. 600 °C (Pekov *et al*. 2007, Macdonald *et al*. 2013, Uher *et al*. 2015, Zozulya *et al*. 2017), whereas the gap is not as clear at higher temperatures (Petrella *et al*. 2014). We thus suggest that the fluorapatite–britholite symplectites formed at or below 600 °C (Fig. 8). Unlike the clear hydrothermally induced formation of the altered apatite (*e.g*., veins and porosity), there is little petrographic evidence to support a hydrothermal origin for the symplectites. This is not surprising, as replacement of fluorapatite commonly occurs on the nano-scale, and the fluid pathways are only observed

using transmission electron microscopy (TEM) imaging (*e.g.*, Harlov *et al*. 2005, Birski *et al*. 2018). There is, however, significant trace element evidence for symplectite formation by hydrothermal fluids. Magnesium and Al are incompatible during igneous crystallization of fluorapatite, evident by their low contents in primary fluorapatite (Fig. 6B). In contrast, hydrothermally altered fluorapatite grains are richer in Mg and Al. The symplectites are similarly rich in Mg and Al, suggesting introduction of these elements by fluids. These elements are probably not in the fluorapatite or britholite crystal structures, but more likely within unobserved nanoscale mineral phases or porosity. Hydrothermal alteration is also evident by the positive Ce anomalies observed for most symplectites (Fig. 6A, C). Figure 6D shows that Ce and Th contents of symplectic fluorapatite are similar to the Ce-Th-richest igneous fluorapatites. Had Ce been introduced to form the anomaly, one would expect Th to be introduced as well, causing both to be higher than observed. Instead, we suggest that LREE except Ce^{4+} were removed from the symplectite, explaining the La and Pr dip observed in Figure 6A. These LREE were likely deposited nearby in the non-stoichiometric britholite-cerite-like phase (Fig. 5A), which also has a strong negative Ce anomaly, consistent with the retention of Ce^{4+} in the symplectites. A similar phase formed in the experiments of Anenburg & Mavrogenes (2018) at temperatures of 550 to 650 °C, within our temperature estimate for symplectite formation.

Comparison with Hoidas Lake

The Hoidas Lake REE deposit in Saskatchewan, Canada (Pandur *et al*. 2014, 2015, 2016) shares many characteristics with Nolans Bore, in that it hosts REE mineralization in veins and dikes of fluorapatite with allanite, diopside, and hyalophane. Both ore deposits are Proterozoic in age and are hosted in granulite-facies metamorphic rocks. In both cases, ore deposition is believed to be from phosphate-rich hydrothermal fluids or evolved melts of carbonatite or alkali association, but no distinct source has been identified. The primary and secondary assemblages in Hoidas Lake are very similar to Nolans Bore and additionally contain hydroxylbastnäsite, hydroxylsynchysite, and ancylite (Pandur *et al*. 2016). Pandur *et al.* (2016) also document REE-rich inclusions in fluorapatite and Ce-rich thorite, features commonly observed in the secondary assemblage at Nolans Bore.

Pandur *et al*. (2014, 2015, 2016) describe a previously unobserved texture involving fluorapatite and REE-rich inclusions with a graphic texture. This texture was mentioned briefly by Pandur *et al*. (2014), elaborated upon by Pandur *et al*. (2015), and was an essential part of a wider genetic model for Hoidas Lake by Pandur *et al*. (2016). The two models given by Pandur *et al*. (2015) involve magmatic processes: (1) crystallization from a boundary layer, similar to equivalent models in granitic pegmatites, or (2) entrapment of two immiscible REE-rich melt fractions in the crystallizing fluorapatite. However, we interpret the texture described by Pandur *et al*. (2015) as two distinct textures: symplectites and hydrothermal alteration, similar to the secondary fluorapatite at Nolans Bore. Pandur *et al*. (2014) document fluid inclusions indicating aqueous alteration at temperatures up to 310 °C, which is consistent with our estimate of hydrothermal overprint at Nolans Bore. In the following sections, we examine each of the claims raised by Pandur *et al*. (2015) to support a magmatic origin for this texture, reinterpret it, and supplement this reinterpretation with observations from Nolans Bore.

Is the texture igneous "graphic" or hydrothermally altered?

Pandur *et al*. (2015) stated that the observed texture is reminiscent of the graphic texture of quartz and feldspar common in granitic pegmatites. These textures are explained as simultaneous growth of quartz and feldspar (Fenn 1986, London 2014, Xu *et al*. 2015). However, the rocks at Hoidas Lake and Nolans Bore are not granitic pegmatites and the minerals comprising this textural association are neither quartz nor feldspar. Furthermore, minerals intergrown in graphic textures commonly have straight or parallel crystal edges and a systematic spatial distribution (Lentz & Fowler 1992).

The interiors of the Hoidas Lake fluorapatite crystals contain fine euhedral intergrowths with a REE-rich phase, texturally identical to our symplectite, whereas the exterior resembles primary igneous fluorapatite overprinted by hydrothermally altered fluorapatite (compare Fig. 2B, C in Pandur *et al*. 2015 and Fig 11 in Pandur *et al*. 2016 with Fig. 1 of this study). Chemical evidence for hydrothermal alteration in Hoidas Lake is evident in Figure 4 of Pandur *et al*. (2015) and Figure 12 of Pandur *et al*. (2016), which show the same La-Ce decoupling observed at Nolans Bore. This is only possible if most of the Ce is quadrivalent, requiring low temperatures and oxidizing conditions. High Ce^{4+}/Ce^{3+} is unlikely at magmatic temperatures, as it requires unrealistically high fO_2, as described above. Specifically, one of their inclusions is a LREE-carbonate (with LREE, C, F, low Ce), and the other is likely to be a mixed carbonate-stetindite (evident by the association of Ce and Si). A third inclusion reported by Pandur *et al*. (2016) is clearly stetindite. Harlov & Förster (2003) demon-

strated that metasomatic monazite after fluorapatite can form rims on the exterior of the original fluorapatite crystal, similar to Figure 2C in Pandur *et al*. (2015).

Shortcomings of the boundary layer model

One of the models suggested by Pandur *et al*. (2015) invokes a boundary layer melt between the bulk melt and the growing crystals: diffusion between the boundary layer and the bulk melt was kinetically limited, causing the boundary layer melt to become depleted in the components forming fluorapatite (*e.g*., Ca, P) and oversaturated in the other components (*e.g*., Si, REE). These oversaturated components crystallized, trapping the solid Si-REE phases as inclusions in the fluorapatite. This model is basically the same as the granitic pegmatite model summarized by London (2014). We claim that the boundary layer model is not applicable to Hoidas Lake or Nolans Bore. Silicon and REE together are compatible in fluorapatite *via* the britholite component coupled substitution $Ca^{2+} + P^{5+} \leftrightarrow REE^{3+} + Si^{4+}$ (Gorbachev *et al*. 2017, Anenburg & Mavrogenes 2018) at magmatic temperatures. The primary mineralization observed at Nolans Bore (and likely Hoidas Lake) is hosted by fluorapatite with a significant britholite component. This leads to a paradox: if the inclusions are representative of a boundary-layer melt enriched in elements that are incompatible in apatite (according to Pandur *et al*. 2015), why do they contain phases in which REE and Si are the major elements? Therefore, the boundary-layer melt model is untenable.

Boundary-layer melts exist in granitic pegmatites because these melts are extremely viscous. The combination of high Si contents and low temperatures result in low diffusion rates, causing the formation of a kinetically controlled graphic texture (London 2014). Furthermore, recent research shows that Li may promote the formation of graphic textures (Maneta & Baker 2014). However, neither Hoidas Lake nor Nolans Bore contain Li-bearing granitic pegmatites. They formed either from a phosphate-bearing carbonatite (Pandur *et al*. 2015, Anenburg & Mavrogenes 2018) or a hydrothermal fluid (Huston *et al*. 2016, Pandur *et al*. 2016). Although an alkali source has been suggested (Huston *et al*. 2016, Pandur *et al*. 2016), there is no clear evidence to support such a source, especially since both deposits are devoid of fenitization. Carbonatites are among the least viscous melts on Earth (Jones *et al*. 2013, Kono *et al*. 2014). Diffusion is so rapid that it is almost impossible to quench them to glass. Experiments involving carbonatites equilibrate in minutes to hours, as opposed to days to weeks for granitic compositions (*e.g*., Wyllie & Tuttle 1960, Wyllie *et al*. 1962, Biggar 1969, Cooper *et al*. 1975, Irving & Wyllie 1975, Lee & Wyllie 2000, Martin *et al*. 2013). A diffusion-controlled boundary layer melt can only exist during rapid crystallization of fluorapatite, but such fluorapatite crystals are commonly needle-like (Wyllie *et al*. 1962) and are not observed at Hoidas Lake or Nolans Bore. Therefore, a diffusion-controlled boundary-layer melt is unlikely to have existed in these melts.

Are the inclusions immiscible melt droplets?

Pandur *et al*. (2015) raised the possibility that the REE-rich solid inclusions are immiscible melt fractions. It is not clear whether their model suggests that the two compositions (Ce-Th-Si-rich and LREE-rich) are conjugate melts or if another melt, not represented in the inclusions, was present. Both cases suffer from the problem of temperature. Pure REE phosphates and silicates have melting points well above 1500 °C (Hikichi & Nomura 1987), and the incorporation of Th or Ce^{4+} will only make these phases more refractory. Fluorine does not act as a flux in this case, as it is an essential component of the solid REE-carbonate, and there is no other F-rich phase in the solid inclusions. Fluxing by water is also not possible because the solubility of REE in H_2O is very low, particularly in the presence of P and the absence of F or Cl (Pourtier *et al*. 2010, Tropper *et al*. 2011, 2013, Zhou *et al*. 2016, Mair *et al*. 2017), and these are hypothesized melt inclusions, not fluid inclusions. Paradoxically, these inclusions melt above the melting point of the host fluorapatite, precluding their origin as liquids trapped in crystallizing fluorapatite. The REE-carbonate observed in the inclusions by Pandur *et al*. (2015, 2016) is unlikely to represent a melt. In all cases where igneous REE-carbonates are observed in natural carbonatites, they are dissolved in a melt dominated by calcite or dolomite components. Also, REE-carbonates are rarely igneous in natural rocks and usually form in late hydrothermal stages of magmatic evolution. They crystallize at relatively low temperatures with an upper limit of about 800 °C, but commonly much lower than 500 °C (Jones & Wyllie 1986, Williams-Jones & Wood 1992, Doroshkevich & Ripp 2004, Ruberti *et al*. 2008, Gysi & Williams-Jones 2015, Verplanck *et al*. 2016, Broom-Fendley *et al*. 2017b, Liu & Hou 2017). Thus, their temperature range of formation is not compatible with the high temperature range for the REE-Th silicates and phosphates and we doubt the coexistence of immiscible liquids with these compositions (carbonates and phosphate-silicates). These hypothesized REE-carbonate-silicate-phosphate melts are not known elsewhere and their existence is suspect.

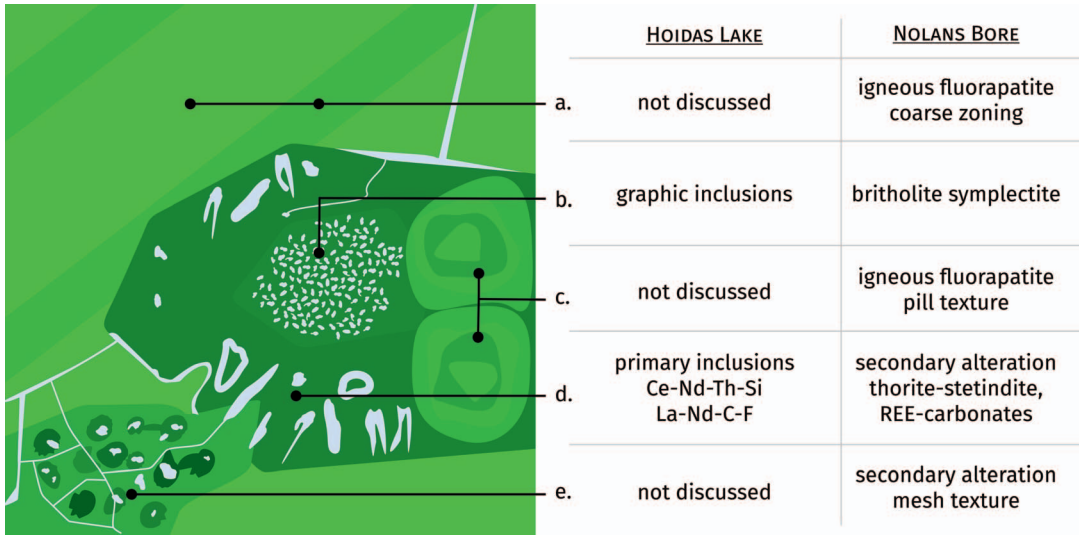

FIG. 9. A schematic sketch of primary and secondary textures discussed here, contrasting the interpretation of textures at Hoidas Lake (Pandur *et al.* 2015, 2016) and Nolans Bore (this study). The sketch is loosely based on Figure 2C of Pandur *et al.* (2015).

Order of fluorapatite crystallization

Pandur *et al*. (2016) reported four generations of fluorapatite: (1–2) *ca*. 1.5–2% REE oxides, inclusion-bearing, Ce-dominant; (3) *ca*. 5.5% REE oxides, inclusion-free, Ce-dominant; and (4) *ca*. 1% REE oxides, inclusion-bearing, Nd-dominant. Based on this order, Pandur *et al*. (2016) proposed a model of changing source fluid or melt conditions. We suggest that the order ought to be: REE-rich and inclusion-free first, followed by REE-poor and inclusion-bearing, as seen at Nolans Bore, where primary igneous assemblages are followed by secondary symplectites and hydrothermal alteration. The Nd-dominant fluorapatite crystallized last, indicating that Ce was oxidized and preferentially sequestered in thorite and stetindite, forming negative Ce anomalies in this late-stage fluorapatite. Interestingly, the Hoidas Lake REE-rich and inclusion-free fluorapatite exhibits both morphologies observed at Nolans Bore: smaller pill-textured and large oscillatory zoned fluorapatite (*e.g.*, bottom right and top of Fig. 2C in Pandur *et al.* 2015, respectively). A summary of the textures observed in Nolans Bore and Hoidas Lake and their interpretation is given in Figure 9.

SIMILAR SYMPLECTITES FROM OTHER LOCALITIES

Symplectites after REE-rich fluorapatite are not unknown. Although the specific assemblage of fluorapatite–britholite in natural rocks has not yet been reported in the literature, other closely related textures are abundant. Examples include monazite-fluorite from the Oktiabrski Massif, Ukraine (Dumańska-Słowik *et al*. 2012, Dumańska-Słowik 2016) and monazite-fluorapatite from the Bohemian Massif, Czech Republic (Finger & Krenn 2007). Non-symplectic inclusions of REE minerals in replaced fluorapatite are also widely known (Harlov *et al*. 2002a, Ziemann *et al*. 2005, Harlov *et al*. 2007a, Torab & Lehmann 2007, Harlov 2011, Jonsson *et al*. 2016, Krneta *et al*. 2016). Specifically, Ali (2012) reports irregularly shaped REE phosphates in apatite. In all cases these textures were interpreted by the authors as metasomatic replacements of apatite, facilitated by hydrothermal alteration.

CONCLUSIONS AND IMPLICATIONS

Primary REE-rich fluorapatite at Nolans Bore was altered in two stages. First, a high-T (~600 °C) exsolution process created a symplectite of REE-poor fluorapatite and britholite. Second, fluid infiltration at lower temperatures (<500 °C) generated a network of patches and veins composed of various Ce-Th-silicates and LREE-carbonates. Cerium was oxidized and consequently decoupled from the rest of the LREE. Almost identical textural and chemical features occur in the Hoidas Lake REE deposit, precluding the magmatic origin suggested by Pandur *et al*. (2015).

Although Nolans Bore experienced several stages of post-magmatic secondary alteration (described here

and by Schoneveld *et al*. 2015), the REE remained mostly contained within Nolans Bore itself and did not migrate into the wall rocks. The REE were sequestered in insoluble phases such as carbonates, silicates, and phosphates, regardless of the ligands that promote REE dissolution (*e.g*., Cl^-). Thus, under the hydrothermal conditions prevailing at Nolans Bore during post-magmatic alteration, REE mobility was limited to the micrometer to millimeter scale (as was observed elsewhere, *e.g*., Förster 2000, Williams-Jones *et al*. 2012). The ore grade of many REE deposits was upgraded by hydrothermal alteration (Andersen *et al*. 2017). However, hydrothermal alteration did not upgrade the ore grade at Nolans Bore, suggesting it is not a significant mineralization process in Nolans-type apatite vein deposits (although the ore grade can be modified by supergene processes; see Schoneveld *et al*. 2015).

The observed variety of REE phases has important implications for theoretical studies of REE transport in hydrothermal fluids (*e.g*., Migdisov *et al*. 2016). REE transport and phase stability is commonly based on the stability of various ligands over a range of fluid pressure-temperature-compositions, but the solubility of complex REE silicates, phosphates, and fluorides is poorly constrained. Solid phases considered in these studies are usually only either well-known phases (monazite, xenotime, apatite, *etc*.), or phases that do not generally occur in nature (simple REE-fluorides). They do not take coexisting phosphates, carbonates, and silicates into consideration, and the potential implications of these assemblages on REE solubility. All insoluble phases must be considered when applying theoretical or simplified experimental studies of REE solubility to natural systems.

Carbonatite-hosted REE deposits are commonly rich in Ce and Th, both of which are undesirable to industry. Cerium is usually the most abundant REE, yet its economic value is low relative to other LREE such as Pr or Nd (2 US$/kg for CeO_2 *versus* 52 US$/kg and 42 US$/kg for Pr_6O_{11} and Nd_2O_3, respectively). Thorium is radioactive and requires special handling procedures (Chen 2011, Haque *et al*. 2014, Zhu *et al*. 2015). Avoiding silicates when designing metal extraction processes could reduce Ce and Th quantities and remove uneconomic trace HREE impurities from an LREE concentrate (*e.g*., Abdel-Khalek 2000). The case of Nolans Bore demonstrates that primary magmatic mineralization and later redistribution of REE and Th during alteration events must be considered during ore deposit evaluation. Furthermore, fluid flow and chemistry—and consequently the particular phases present—might vary spatially throughout a deposit. The economic value of specific portions of a deposit can depend on this variability, even though the bulk composition is the same.

Acknowledgments

This research is supported by an Australian Government Research Training Program (RTP) Scholarship and a Ringwood Scholarship from the Research School of Earth Sciences, Australian National University to Michael Anenburg. Financial support by Arafura Resources is gratefully acknowledged. Access to the facilities of the ACT Node of the Australian National Fabrication Facility (ANFF) and Centre for Advanced Microscopy (CAM), with funding through the Australian Microscopy and Microanalysis Research Facility (AMMRF), is gratefully acknowledged. We thank Daniel Harlov and an anonymous reviewer for their comments that allowed us to improve the manuscript.

References

Abdel-Khalek, N.A. (2000) Evaluation of flotation strategies for sedimentary phosphates with siliceous and carbonates gangues. *Minerals Engineering* **13**, 789–793.

Ali, M.A. (2012) Mineral chemistry of monazite-(Nd), xenotime-(Y), apatite, fluorite and zircon hosting in lamprophyre dyke in Abu Rusheid area, South Eastern Desert, Egypt. *Geologija* **55**, 93–105.

Andersen, A.K., Clark, J.G., Larson, P.B., & Neill, O.K. (2016) Mineral chemistry and petrogenesis of a HFSE(+HREE) occurrence, peripheral to carbonatites of the Bear Lodge alkaline complex, Wyoming. *American Mineralogist* **101**, 1604–1623.

Andersen, A.K., Clark, J.G., Larson, P.B., & Donovan, J.J. (2017) REE fractionation, mineral speciation, and supergene enrichment of the Bear Lodge carbonatites, Wyoming, USA. *Ore Geology Reviews* **89**, 780–807.

Anderson, J.R., Kelsey, D.E., Hand, M., & Collins, W.J. (2013) Conductively driven, high-thermal gradient metamorphism in the Anmatjira Range, Arunta region, central Australia. *Journal of Metamorphic Geology* **31**, 1003–1026.

Andrade, F.R.D., Möller, P., Lüders, V., Dulski, P., & Gilg, H.A. (1999) Hydrothermal rare earth elements mineralization in the Barra do Itapirapuã carbonatite, southern Brazil: behaviour of selected trace elements and stable isotopes (C, O). *Chemical Geology* **155**, 91–113.

Anenburg, M. & Mavrogenes, J.A. (2018) Carbonatitic versus hydrothermal origin for fluorapatite REE-Th deposits: Experimental study of REE transport and crustal "antiskarn" metasomatism. *American Journal of Science* **318**, 335–366.

Atwood, D.A. (2012) *The rare earth elements: fundamentals and applications*. John Wiley & Sons, New Jersey, United States.

Ballard, J.R., Palin, J.M., & Campbell, I.H. (2002) Relative oxidation states of magmas inferred from Ce(IV)/Ce(III) in zircon: application to porphyry copper deposits of northern Chile. *Contributions to Mineralogy and Petrology* **144**, 347–364.

Belousova, E.A., Griffin, W.L., O'Reilly, S.Y., & Fisher, N.I. (2002) Igneous zircon: trace element composition as an indicator of source rock type. *Contributions to Mineralogy and Petrology* **143**, 602–622.

Berger, A., Gnos, E., Janots, E., Fernandez, A., & Giese, J. (2008) Formation and composition of rhabdophane, bastnäsite and hydrated thorium minerals during alteration: Implications for geochronology and low-temperature processes. *Chemical Geology* **254**, 238–248.

Betkowski, W.B., Harlov, D.E., & Rakovan, J.F. (2016) Hydrothermal mineral replacement reactions for an apatite-monazite assemblage in alkali-rich fluids at 300–600 °C and 100 MPa. *American Mineralogist* **101**, 2620–2637.

Biermeier, C., Stüwe, K., Foster, D.A., & Finger, F. (2003) Thermal evolution of the Redbank thrust system, central Australia: Geochronological and phase-equilibrium constraints. *Tectonics* **22**, 23 pp.

Biggar, G.M. (1969) Phase relationships in the join $Ca(OH)_2$–$CaCO_3$–$Ca_3(PO_4)_2$–H_2O at 1000 bars. *Mineralogical Magazine* **37**, 75–82.

Birski, Ł., Wirth, R., Słaby, E., Wudarska, A., Lepland, A., Hofmann, A., & Schreiber, A. (2018) (Ca-Y)-phosphate inclusions in apatite crystals from Archean rocks from the Barberton Greenstone Belt and Pilbara Craton: First report of natural occurrence. *American Mineralogist* **103**, 307–313.

Blundy, J. & Wood, B. (2003) Partitioning of trace elements between crystals and melts. *Earth and Planetary Science Letters* **210**, 383–397.

Bodeving, S., Williams-Jones, A.E., & Swinden, S. (2017) Carbonate–silicate melt immiscibility, REE mineralising fluids, and the evolution of the Lofdal Intrusive Suite, Namibia. *Lithos* **268**–**271**, 383–398.

Boyer, L. (1997) Synthesis of phosphate-silicate apatites at atmospheric pressure. *Solid State Ionics* **95**, 121–129.

Brassinnes, S., Balaganskaya, E., & Demaiffe, D. (2005) Magmatic evolution of the differentiated ultramafic, alkaline and carbonatite intrusion of Vuoriyarvi (Kola Peninsula, Russia). A LA-ICP-MS study of apatite. *Lithos* **85**, 76–92.

Broom-Fendley, S., Brady, A.E., Horstwood, M.S.A., Woolley, A.R., Mtegha, J., Wall, F., Dawes, W., & Gunn, G. (2017a) Geology, geochemistry and geochronology of the Songwe Hill carbonatite, Malawi. *Journal of African Earth Sciences* **134**, 10–23.

Broom-Fendley, S., Brady, A.E., Wall, F., Gunn, G., & Dawes, W. (2017b) REE minerals at the Songwe Hill carbonatite, Malawi: HREE-enrichment in late-stage apatite. *Ore Geology Reviews* **81**, 23–41.

Budzyń, B., Harlov, D.E., Williams, M.L., & Jercinovic, M.J. (2011) Experimental determination of stability relations between monazite, fluorapatite, allanite, and REE-epidote as a function of pressure, temperature, and fluid composition. *American Mineralogist* **96**, 1547–1567.

Budzyń, B., Harlov, D.E., Kozub-Budzyń, G.A., & Majka, J. (2017) Experimental constraints on the relative stabilities of the two systems monazite-(Ce)–allanite-(Ce)–fluorapatite and xenotime-(Y)–(Y,HREE)-rich epidote–(Y,HREE)-rich fluorapatite, in high Ca and Na-Ca environments under P-T conditions of 200–1000 MPa and 450–750 °C. *Mineralogy and Petrology* **111**, 183–217.

Bühn, B. (2008) The role of the volatile phase for REE and Y fractionation in low-silica carbonate magmas: implications from natural carbonatites, Namibia. *Mineralogy and Petrology* **92**, 453–470.

Buick, I.S., Storkey, A., & Williams, I.S. (2008) Timing relationships between pegmatite emplacement, metamorphism and deformation during the intra-plate Alice Springs Orogeny, central Australia. *Journal of Metamorphic Geology* **26**, 915–936.

Burnham, A.D. & Berry, A.J. (2012) An experimental study of trace element partitioning between zircon and melt as a function of oxygen fugacity. *Geochimica et Cosmochimica Acta* **95**, 196–212.

Chakhmouradian, A.R. & Wall, F. (2012) Rare earth elements: minerals, mines, magnets (and more). *Elements* **8**, 333–340.

Chakhmouradian, A.R. & Zaitsev, A.N. (2012) Rare earth mineralization in igneous rocks: sources and processes. *Elements* **8**, 347–353.

Chakhmouradian, A.R., Reguir, E.P., Zaitsev, A.N., Couëslan, C., Xu, C., Kynický, J., Mumin, A.H., & Yang, P. (2017) Apatite in carbonatitic rocks: Compositional variation, zoning, element partitioning and petrogenetic significance. *Lithos* **274**–**275**, 188–213.

Chen, Z. (2011) Global rare earth resources and scenarios of future rare earth industry. *Journal of Rare Earths* **29**, 1–6.

Claoué-Long, J., Edgoose, C., & Worden, K. (2008) A correlation of Aileron Province stratigraphy in central Australia. *Precambrian Research* **166**, 230–245.

Cooper, A.F., Gittins, J., & Tuttle, O.F. (1975) The system Na_2CO_3–K_2CO_3–$CaCO_3$ at 1 kilobar and its significance in carbonatite petrogenesis. *American Journal of Science* **275**, 534–560.

Cooper, A.F., Collins, A.K., Palin, J.M., & Spratt, J. (2015) Mineralogical evolution and REE mobility during crystallisation of ancylite-bearing ferrocarbonatite, Haast River, New Zealand. *Lithos* **216**–**217**, 324–337.

Decrée, S., Boulvais, P., Tack, L., André, L., & Baele, J.-M. (2016). Fluorapatite in carbonatite-related phosphate deposits: the case of the Matongo carbonatite (Burundi). *Mineralium Deposita* **51**, 453–466.

Dirks, P.H.G.M., Hand, M., & Powell, R. (1991) The *P–T–* deformation path for a mid-Proterozoic, low-pressure terrane: the Reynolds Range, central Australia. *Journal of Metamorphic Geology* **9**, 641–661.

Doroshkevich, A.G. & Ripp, G.S. (2004) Estimation of the conditions of formation of REE-carbonatites in western Transbaikalia. *Russian Geology and Geophysics* **45**, 492–500.

Doroshkevich, A.G., Viladkar, S.G., Ripp, G.S., & Burtseva, M.V. (2009) Hydrothermal REE mineralization in the Amba Dongar carbonatite complex, Gujarat, India. *Canadian Mineralogist* **47**, 1105–1116.

Dumańska-Słowik, M. (2016) Evolution of mariupolite (nepheline syenite) in the alkaline Oktiabrski Massif (Ukraine) as the host of potential Nb–Zr–REE mineralization. *Ore Geology Reviews* **78**, 1–13.

Dumańska-Słowik, M., Budzyń, B., Heflik, W., & Sikorska, M. (2012) Stability relationships of REE-bearing phosphates in an alkali-rich system (nepheline syenite from the Mariupol Massif, SE Ukraine). *Acta Geologica Polonica* **62**.

Eggins, S.M., Kinsley, L.P.J., & Shelley, J.M.G. (1998) Deposition and element fractionation processes during atmospheric pressure laser sampling for analysis by ICP-MS. *Applied Surface Science* **127–129**, 278–286.

Ermolaeva, V.N., Pekov, I.V., Chukanov, N.V., & Zadov, A.E. (2007) Thorium mineralization in hyperalkaline pegmatites and hydrothermalites of the Lovozero pluton, Kola Peninsula. *Geology of Ore Deposits* **49**, 758–775.

Feng, M., Xu, C., Kynicky, J., Zeng, L., & Song, W. (2016) Rare earth element enrichment in Palaeoproterozoic Fengzhen carbonatite from the North China block. *International Geology Review* **58**, 1940–1950.

Fenn, P.M. (1986) On the origin of graphic granite. *American Mineralogist* **71**, 325–330.

Finger, F. & Krenn, E. (2007) Three metamorphic monazite generations in a high-pressure rock from the Bohemian Massif and the potentially important role of apatite in stimulating polyphase monazite growth along a PT loop. *Lithos* **95**, 103–115.

Förster, H.-J. (2000) Cerite-(Ce) and thorian synchysite-(Ce) from the Niederbobritzsch granite, Erzgebirge, Germany: implications for the differential mobility of the LREE and Th during alteration. *Canadian Mineralogist* **38**, 67–79.

Förster, H.-J. (2006) Composition and origin of intermediate solid solutions in the system thorite–xenotime–zircon–coffinite. *Lithos* **88**, 35–55.

Gaidies, F., Milke, R., Heinrich, W., & Abart, R. (2017) Metamorphic mineral reactions: Porphyroblast, corona and symplectite growth. *In* Mineral reaction kinetics: Microstructures, textures, chemical and isotopic signatures (W. Heinrich & R. Abart, eds.). European Mineralogical Union (469–540).

Gorbachev, N.S., Shapovalov, Y.B., & Kostyuk, A.V. (2017) Experimental study of the apatite–carbonate–H_2O system at $P = 0.5$ GPa and $T = 1200$ °C: Efficiency of fluid transport in carbonatite. *Doklady Earth Sciences* **473**, 350–353.

Gros, K., Słaby, E., Förster, H.-J., Michalak, P.P., Munnik, F., Götze, J., & Rhede, D. (2016) Visualization of trace-element zoning in fluorapatite using BSE and CL imaging, and EPMA and μPIXE/μPIGE mapping. *Mineralogy and Petrology* **110**, 809–821.

Gysi, A.P. & Williams-Jones, A.E. (2015) The thermodynamic properties of bastnäsite-(Ce) and parisite-(Ce). *Chemical Geology* **392**, 87–101.

Haines, P.W., Hand, M., & Sandiford, M. (2001) Palaeozoic synorogenic sedimentation in central and northern Australia: A review of distribution and timing with implications for the evolution of intracontinental orogens. *Australian Journal of Earth Sciences* **48**, 911–928.

Hammouda, T., Chantel, J., & Devidal, J.-L. (2010) Apatite solubility in carbonatitic liquids and trace element partitioning between apatite and carbonatite at high pressure. *Geochimica et Cosmochimica Acta* **74**, 7220–7235.

Hand, M. & Sandiford, M. (1999) Intraplate deformation in central Australia, the link between subsidence and fault reactivation. *Tectonophysics* **305**, 121–140.

Haque, N., Hughes, A., Lim, S., & Vernon, C. (2014) Rare earth elements: Overview of mining, mineralogy, uses, sustainability and environmental impact. *Resources* **3**, 614–635.

Harlov, D.E. (2011) Formation of monazite and xenotime inclusions in fluorapatite megacrysts, Gloserheia Granite Pegmatite, Froland, Bamble Sector, southern Norway. *Mineralogy and Petrology* **102**, 77–86.

Harlov, D.E. & Förster, H.-J. (2003) Fluid-induced nucleation of (Y+REE)-phosphate minerals within apatite: Nature and experiment. Part II. Fluorapatite. *American Mineralogist* **88**, 1209–1229.

Harlov, D.E., Andersson, U.B., Förster, H.-J., Nyström, J.O., Dulski, P., & Broman, C. (2002a) Apatite–monazite relations in the Kiirunavaara magnetite–apatite ore, northern Sweden. *Chemical Geology* **191**, 47–72.

Harlov, D.E., Förster, H.-J., & Nijland, T.G. (2002b) Fluid-induced nucleation of (Y + REE)-phosphate minerals within apatite: Nature and experiment. Part I. Chlorapatite. *American Mineralogist* **87**, 245–261.

Harlov, D.E., Wirth, R., & Förster, H.-J. (2005) An experimental study of dissolution–reprecipitation in fluorapatite: fluid infiltration and the formation of monazite. *Contributions to Mineralogy and Petrology* **150**, 268–286.

Harlov, D.E., Marschall, H.R., & Hanel, M. (2007a) Fluorapatite-monazite relationships in granulite-facies metapelites, Schwarzwald, southwest Germany. *Mineralogical Magazine* **71**, 223–234.

Harlov, D.E., Wirth, R., & Hetherington, C.J. (2007b) The relative stability of monazite and huttonite at 300–900 °C

and 200–1000 MPa: Metasomatism and the propagation of metastable mineral phases. *American Mineralogist* **92**, 1652–1664.

Hikichi, Y. & Nomura, T. (1987) Melting temperatures of monazite and xenotime. *Journal of the American Ceramic Society* **70**, C-252–C-253.

Hoatson, D.M., Jaireth, S., & Miezitis, Y. (2011) *The major rare-earth-element deposits of Australia: geological setting, exploration, and resources*. Geoscience Australia.

Holtstam, D. & Andersson, U.B. (2007) The REE minerals of the Bastnäs-type deposits, south-central Sweden. *Canadian Mineralogist* **45**, 1073–1114.

Huston, D.L., Maas, R., Cross, A., Hussey, K.J., Mernagh, T.P., Fraser, G., & Champion, D.C. (2016) The Nolans Bore rare-earth element-phosphorus-uranium mineral system: geology, origin and post-depositional modifications. *Mineralium Deposita* **51**, 797–822.

Irving, A.J. & Wyllie, P.J. (1975) Subsolidus and melting relationships for calcite, magnesite and the join $CaCO_3$–$MgCO_3$ 36 kb. *Geochimica et Cosmochimica Acta* **39**, 35–53.

Jones, A.P. & Wyllie, P.J. (1986) Solubility of rare earth elements in carbonatite magmas, indicated by the liquidus surface in $CaCO_3$–$Ca(OH)_2$–$La(OH)_3$ at 1 kbar pressure. *Applied Geochemistry* **1**, 95–102.

Jones, A.P., Genge, M., & Carmody, L. (2013) Carbonate melts and carbonatites. *Reviews in Mineralogy and Geochemistry* **75**, 289–322.

Jonsson, E., Harlov, D.E., Majka, J., Högdahl, K., & Persson-Nilsson, K. (2016) Fluorapatite-monazite-allanite relations in the Grängesberg apatite-iron oxide ore district, Bergslagen, Sweden. *American Mineralogist* **101**, 1769–1782.

Klimm, K., Kohn, S.C., & Botcharnikov, R.E. (2012) The dissolution mechanism of sulphur in hydrous silicate melts. II: Solubility and speciation of sulphur in hydrous silicate melts as a function of fO_2. *Chemical Geology* **322**–**323**, 250–267.

Kono, Y., Kenney-Benson, C., Hummer, D., Ohfuji, H., Park, C., Shen, G., Wang, Y., Kavner, A., & Manning, C.E. (2014) Ultralow viscosity of carbonate melts at high pressures. *Nature Communications* **5**, 5091.

Krneta, S., Ciobanu, C.L., Cook, N.J., Ehrig, K., & Kontonikas-Charos, A. (2016) Apatite at Olympic Dam, South Australia: A petrogenetic tool. *Lithos* **262**, 470–485.

Langmuir, D. (1978) Uranium solution–mineral equilibria at low temperatures with applications to sedimentary ore deposits. *Geochimica et Cosmochimica Acta* **42**, 547–569.

Latham, S., Varslot, T., & Sheppard, A. (2008) Automated registration for augmenting micro-CT 3D images. *ANZIAM Journal (CTAC2008)* **50**, C534–C548.

Lee, W.J. & Wyllie, P.J. (2000) The system CaO–MgO–SiO_2–CO_2 at 1 GPa, metasomatic wehrlites, and primary carbonatite magmas. *Contributions to Mineralogy and Petrology* **138**, 214–228.

Lentz, D.R. & Fowler, A.D. (1992) A dynamic model for graphic quartz–feldspar intergrowths in granitic pegmatites in the southwestern Grenville Province. *Canadian Mineralogist* **30**, 571–585.

Li, X. & Zhou, M.-F. (2015) Multiple stages of hydrothermal REE remobilization recorded in fluorapatite in the Paleoproterozoic Yinachang Fe–Cu–(REE) deposit, Southwest China. *Geochimica et Cosmochimica Acta* **166**, 53–73.

Limaye, A. (2012) Drishti: a volume exploration and presentation tool. Proceedings of the SPIE 8506, *Developments in X-Ray Tomography VIII*, 85060X.

Linnen, R.L., Samson, I.M., Williams-Jones, A.E., & Chakhmouradian, A.R. (2014) Geochemistry of the rare-earth element, Nb, Ta, Hf, and Zr deposits. *In* Treatise on Geochemistry, Second Edition (S.D. Scott, ed.). Elsevier Science (543–568).

Liu, Y. & Hou, Z. (2017) A synthesis of mineralization styles with an integrated genetic model of carbonatite-syenite-hosted REE deposits in the Cenozoic Mianning-Dechang REE metallogenic belt, the eastern Tibetan Plateau, southwestern China. *Journal of Asian Earth Sciences* **137**, 35–79.

London, D. (2014) A petrologic assessment of internal zonation in granitic pegmatites. *Lithos* **184**–**187**, 74–104.

Lottermoser, B.G. (1990) Rare-earth element mineralisation within the Mt. Weld carbonatite laterite, Western Australia. *Lithos* **24**, 151–167.

Lupulescu, M.V., Hughes, J.M., Chiarenzelli, J.R., & Bailey, D.G. (2017) Texture, crystal structure, and composition of fluorapatites from iron oxide-apatite (IOA) deposits, eastern Adirondack Mountains, New York. *Canadian Mineralogist* **55**, 399–417.

Macdonald, R., Bagiński, B., Dzierżanowski, P., & Jokubauskas, P. (2013) Apatite-supergroup minerals in UK Palaeogene granites: composition and relationship to host-rock composition. *European Journal of Mineralogy* **25**, 461–471.

Macdonald, R., Bagiński, B., Kartashov, P.M., & Zozulya, D. (2017a) Behaviour of $ThSiO_4$ during hydrothermal alteration of rare-metal rich lithologies from peralkaline rocks. *Mineralogical Magazine* **81**, 873–893.

Macdonald, R., Bagiński, B., & Zozulya, D. (2017b) Differing responses of zircon, chevkinite-(Ce), monazite-(Ce) and fergusonite-(Y) to hydrothermal alteration: Evidence from the Keivy alkaline province, Kola Peninsula, Russia. *Mineralogy and Petrology* **111**, 523–545.

Mair, P., Tropper, P., Harlov, D.E., & Manning, C.E. (2017) The solubility of $CePO_4$ monazite and YPO_4 xenotime in KCl-H_2O fluids at 800 °C and 1.0 GPa: Implications for REE transport in high-grade crustal fluids. *American Mineralogist* **102**, 2457–2466.

Maneta, V. & Baker, D.R. (2014) Exploring the effect of lithium on pegmatitic textures: An experimental study. *American Mineralogist* **99**, 1383–1403.

Martin, L.H.J., Schmidt, M.W., Mattsson, H.B., & Guenther, D. (2013) Element partitioning between immiscible carbonatite and silicate melts for dry and H_2O-bearing systems at 1–3 GPa. *Journal of Petrology* **54**, 2301–2338.

Matjuschkin, V., Blundy, J.D., & Brooker, R.A. (2016) The effect of pressure on sulphur speciation in mid- to deep-crustal arc magmas and implications for the formation of porphyry copper deposits. *Contributions to Mineralogy and Petrology* **171**, 66.

Meintzer, R.E. & Mitchell, R.S. (1988) The epigene alteration of allanite. *Canadian Mineralogist* **26**, 945–955.

Migdisov, A.A. & Williams-Jones, A.E. (2014) Hydrothermal transport and deposition of the rare earth elements by fluorine-bearing aqueous liquids. *Mineralium Deposita* **49**, 987–997.

Migdisov, A., Williams-Jones, A.E., Brugger, J., & Caporuscio, F.A. (2016) Hydrothermal transport, deposition, and fractionation of the REE: Experimental data and thermodynamic calculations. *Chemical Geology* **439**, 13–42.

Moore, M., Chakhmouradian, A.R., Mariano, A.N., & Sidhu, R. (2015) Evolution of rare-earth mineralization in the Bear Lodge carbonatite, Wyoming: Mineralogical and isotopic evidence. *Ore Geology Reviews* **64**, 499–521.

Morrissey, L.J., Hand, M., Raimondo, T., & Kelsey, D.E. (2014) Long-lived high-*T*, low-*P* granulite facies metamorphism in the Arunta Region, central Australia. *Journal of Metamorphic Geology* **32**, 25–47.

Myers, G.R., Kingston, A.M., Varslot, T.K., & Sheppard, A.P. (2011) Extending reference scan drift correction to high-magnification high-cone-angle tomography. *Optics Letters* **36**, 4809–4811.

Nadeau, O., Cayer, A., Pelletier, M., Stevenson, R., & Jébrak, M. (2015) The Paleoproterozoic Montviel carbonatite-hosted REE–Nb deposit, Abitibi, Canada: Geology, mineralogy, geochemistry and genesis. *Ore Geology Reviews* **67**, 314–335.

Narasayya, B.L. & Sriramadas, A. (1974) Apatite from apatite-magnetite deposits of Kasipatnam, Andhra Pradesh. *Proceedings of the Indian Academy of Sciences - Section A* **80**, 207–210.

Oberti, R., Ottolini, L., Ventura, G.D., & Parodi, G.C. (2001) On the symmetry and crystal chemistry of britholite: New structural and microanalytical data. *American Mineralogist* **86**, 1066–1075.

Ondrejka, M., Putiš, M., Uher, P., Schmiedt, I., Pukančík, L., & Konečný, P. (2016) Fluid-driven destabilization of REE-bearing accessory minerals in the granitic orthogneisses of North Veporic basement (Western Carpathians, Slovakia). *Mineralogy and Petrology* **110**, 561–580.

O'Neill, H.S.C. (2016) The smoothness and shapes of chondrite-normalized rare earth element patterns in basalts. *Journal of Petrology* **57**, 1463–1508.

Onuma, N., Higuchi, H., Wakita, H., & Nagasawa, H. (1968) Trace element partition between two pyroxenes and the host lava. *Earth and Planetary Science Letters* **5**, 47–51.

Pan, Y., Fleet, M.E., & Macrae, N.D. (1993) Oriented monazite inclusions in apatite porphyroblasts from the Hemlo gold deposit, Ontario, Canada. *Mineralogical Magazine* **57**, 697–707.

Pandur, K., Kontak, D.J., & Ansdell, K.M. (2014) Hydrothermal evolution in the Hoidas Lake vein-type REE deposit, Saskatchewan, Canada: constraints from fluid inclusion microthermometry and evaporate mound analysis. *Canadian Mineralogist* **52**, 717–744.

Pandur, K., Ansdell, K.M., & Kontak, D.J. (2015) Graphic-textured inclusions in apatite: Evidence for pegmatitic growth in a REE-enriched carbonatitic system. *Geology* **43**, 547–550.

Pandur, K., Ansdell, K.M., Kontak, D.J., Halpin, K.M., & Creighton, S. (2016) Petrographic and mineral chemical characteristics of the Hoidas Lake deposit, northern Saskatchewan, Canada: constraints on the origin of a distal magmatic-hydrothermal REE system. *Economic Geology* **111**, 667–694.

Paton, C., Hellstrom, J., Paul, B., Woodhead, J., & Hergt, J. (2011) Iolite: Freeware for the visualisation and processing of mass spectrometric data. *Journal of Analytical Atomic Spectrometry* **26**.

Paul, A. & Douglas, R.W. (1965) Cerous-ceric equilibrium in binary alkali borate and alkali silicate glasses. *Physics and Chemistry of Glasses* **6**, 212–215.

Pekov, I.V., Pasero, M., Yaskovskaya, A.N., Chukanov, N.V., Pushcharovsky, D.Y., Merlino, S., Zubkova, N.V., Kononkova, N.N., Men'shikov, Y.P., & Zadov, A.E. (2007) Fluorcalciobritholite, $(Ca,REE)_5[(Si,P)O_4]_3F$, a new mineral: description and crystal chemistry. *European Journal of Mineralogy* **19**, 95–103.

Petrella, L., Williams-Jones, A.E., Goutier, J., & Walsh, J. (2014) The Nature and Origin of the Rare Earth Element Mineralization in the Misery Syenitic Intrusion, Northern Québec, Canada. *Economic Geology* **109**, 1643–1666.

Pettke, T., Audétat, A., Schaltegger, U., & Heinrich, C.A. (2005) Magmatic-to-hydrothermal crystallization in the W–Sn mineralized Mole Granite (NSW, Australia). *Chemical Geology* **220**, 191–213.

Pourtier, E., Devidal, J.-L., & Gibert, F. (2010) Solubility measurements of synthetic neodymium monazite as a function of temperature at 2 kbars, and aqueous neodymium speciation in equilibrium with monazite. *Geochimica et Cosmochimica Acta* **74**, 1872–1891.

Prokopyev, I.R., Doroshkevich, A.G., Ponomarchuk, A.V., & Sergeev, S.A. (2017) Mineralogy, age and genesis of apatite-dolomite ores at the Seligdar apatite deposit (Central Aldan, Russia). *Ore Geology Reviews* **81**, 296–308.

Pyle, J.M., Spear, F.S., & Wark, D.A. (2002) Electron microprobe analysis of REE in apatite, monazite and xenotime: Protocols and pitfalls. *Reviews in Mineralogy and Geochemistry* **48**, 337–362.

Raimondo, T., Clark, C., Hand, M., & Faure, K. (2011) Assessing the geochemical and tectonic impacts of fluid–rock interaction in mid-crustal shear zones: A case study from the intracontinental Alice Springs Orogen, central Australia. *Journal of Metamorphic Geology* **29**, 821–850.

Raimondo, T., Clark, C., Hand, M., Cliff, J., & Harris, C. (2012) High-resolution geochemical record of fluid–rock interaction in a mid-crustal shear zone: a comparative study of major element and oxygen isotope transport in garnet. *Journal of Metamorphic Geology* **30**, 255–280.

Reed, S.J.B. (2006) *Electron Microprobe Analysis and Scanning Electron Microscopy in Geology*. Cambridge University Press, 232 pp.

Ruberti, E., Enrich, G.E.R., Gomes, C.B., & Comin-Chiaramonti, P. (2008) Hydrothermal REE fluorocarbonate mineralization at Barra Do Itapirapuã, a multiple stockwork carbonatite, Southern Brazil. *Canadian Mineralogist* **46**, 901–914.

Savelyeva, V.B., Demonterova, E.I., Danilova, Y.V., Bazarova, E.P., Ivanov, A.V., & Kamenetsky, V.S. (2016) New carbonatite complex in the western Baikal area, southern Siberian craton: Mineralogy, age, geochemistry, and petrogenesis. *Petrology* **24**, 271–302.

Savelyeva, V.B., Bazarova, E.P., Sharygin, V.V., Karmanov, N.S., & Kanakin, S.V. (2017) Altered rocks of the Onguren carbonatite complex in the Western Tansbaikal Region: Geochemistry and composition of accessory minerals. *Geology of Ore Deposits* **59**, 315–340.

Schoneveld, L., Spandler, C., & Hussey, K. (2015) Genesis of the central zone of the Nolans Bore rare earth element deposit, Northern Territory, Australia. *Contributions to Mineralogy and Petrology* **170**, 11.

Scrimgeour, I.R. (2013) Aileron Province. *In* Geology and mineral resources of the Northern Territory (M. Ahmad & T.J. Munson, eds.). Northern Territory Geological Survey (12.11–12.74).

Seydoux-Guillaume, A.-M., Montel, J.-M., Bingen, B., Bosse, V., de Parseval, P., Paquette, J.-L., Janots, E., & Wirth, R. (2012) Low-temperature alteration of monazite: Fluid mediated coupled dissolution–precipitation, irradiation damage, and disturbance of the U–Pb and Th–Pb chronometers. *Chemical Geology* **330**–**331**, 140–158.

Shaw, R.D. & Black, L.P. (1991) The history and tectonic implications of the Redbank Thrust Zone, central Australia, based on structural, metamorphic and Rb-Sr isotopic evidence. *Australian Journal of Earth Sciences* **38**, 307–332.

Smythe, D.J. & Brenan, J.M. (2016) Magmatic oxygen fugacity estimated using zircon-melt partitioning of cerium. *Earth and Planetary Science Letters* **453**, 260–266.

Spruzeniece, L., Piazolo, S., Daczko, N.R., Kilburn, M.R., & Putnis, A. (2017) Symplectite formation in the presence of a reactive fluid: insights from hydrothermal experiments. *Journal of Metamorphic Geology* **35**, 281–299.

Torab, F.M. & Lehmann, B. (2007) Magnetite-apatite deposits of the Bafq district, Central Iran: apatite geochemistry and monazite geochronology. *Mineralogical Magazine* **71**, 347–363.

Trail, D., Watson, E.B., & Tailby, N.D. (2011) The oxidation state of Hadean magmas and implications for early Earth's atmosphere. *Nature* **480**, 79–82.

Trofanenko, J., Williams-Jones, A.E., Simandl, G.J., & Migdisov, A.A. (2016) The nature and origin of the REE mineralization in the Wicheeda Carbonatite, British Columbia, Canada. *Economic Geology* **111**, 199–223.

Tropper, P., Manning, C.E., & Harlov, D.E. (2011) Solubility of $CePO_4$ monazite and YPO_4 xenotime in H_2O and H_2O–NaCl at 800 °C and 1 GPa: Implications for REE and Y transport during high-grade metamorphism. *Chemical Geology* **282**, 58–66.

Tropper, P., Manning, C.E., & Harlov, D.E. (2013) Experimental determination of $CePO_4$ and YPO_4 solubilities in H_2O-NaF at 800 °C and 1 GPa: Implications for rare earth element transport in high-grade metamorphic fluids. *Geofluids* **13**, 372–380.

Uher, P., Ondrejka, M., Bačík, P., Broska, I., & Konečný, P. (2015) Britholite, monazite, REE carbonates, and calcite: Products of hydrothermal alteration of allanite and apatite in A-type granite from Stupné, Western Carpathians, Slovakia. *Lithos* **236**–**237**, 212–225.

Varslot, T., Kingston, A., Myers, G., & Sheppard, A. (2011) High-resolution helical cone-beam micro-CT with theoretically-exact reconstruction from experimental data. *Medical Physics* **38**, 5459–5476.

Verplanck, P.L., Mariano, A.N., & Mariano, A., Jr. (2016) *Rare earth element ore geology of carbonatites* (P.L. Verplanck & M.W. Hitzman, eds.). Society of Economic Geologists (5–32).

Vry, J., Compston, W., & Cartwright, I. (1996) SHRIMP II dating of zircons and monazites: reassessing the timing of high-grade metamorphism and fluid flow in the Reynolds Range, northern Arunta Block, Australia. *Journal of Metamorphic Geology* **14**, 335–350.

Wall, F. (2014) Rare earth elements. *In* Critical Metals Handbook (G. Gunn, ed.). John Wiley & Sons (312–339).

Waychunas, G.A. (2002) Apatite luminescence. *Reviews in Mineralogy and Geochemistry* **48**, 701–742.

Williams-Jones, A.E. & Wood, S.A. (1992) A preliminary petrogenetic grid for REE fluorocarbonates and associated minerals. *Geochimica et Cosmochimica Acta* **56**, 725–738.

Williams-Jones, A.E., Migdisov, A.A., & Samson, I.M. (2012) Hydrothermal mobilisation of the rare earth

rlements – a tale of "Ceria" and "Yttria". *Elements* **8**, 355–360.

Wolf, M.B. & London, D. (1995) Incongruent dissolution of REE- and Sr-rich apatite in peraluminous granitic liquids; differential apatite, monazite, and xenotime solubilities during anatexis. *American Mineralogist* **80**, 765–775.

Woodhead, J.D., Hellstrom, J., Hergt, J.M., Greig, A., & Maas, R. (2007) Isotopic and elemental imaging of geological materials by laser ablation inductively coupled plasma-mass spectrometry. *Geostandards and Geoanalytical Research* **31(4)**, 331–343.

Wyllie, P.J. & Tuttle, O.F. (1960) The system $CaO–CO_2–H_2O$ and the origin of carbonatites. *Journal of Petrology* **1**, 1–46.

Wyllie, P.J., Cox, K.G., & Biggar, G.M. (1962) The habit of apatite in synthetic systems and igneous rocks. *Journal of Petrology* **3**, 238–243.

Xu, H., Zhang, J., Yu, T., Rivers, M., Wang, Y., & Zhao, S. (2015) Crystallographic evidence for simultaneous growth in graphic granite. *Gondwana Research* **27**, 1550–1559.

Xu, C., Kynický, J., Smith, M.P., Kopriva, A., Brtnický, M., Urubek, T., Yang, Y., Zhao, Z., He, C., & Song, W. (2017) Origin of heavy rare earth mineralization in South China. *Nature Communications* **8**, 14598.

Zeng, L.-P., Zhao, X.-F., Li, X.-C., Hu, H., & McFarlane, C. (2016) *In situ* elemental and isotopic analysis of fluorapatite from the Taocun magnetite-apatite deposit, Eastern China: Constraints on fluid metasomatism. *American Mineralogist* **101**, 2468–2483.

Zhou, L., Mavrogenes, J., Spandler, C., & Li, H. (2016) A synthetic fluid inclusion study of the solubility of monazite-(La) and xenotime-(Y) in H_2O-Na-K-Cl-F-CO_2 fluids at 800 °C and 0.5 GPa. *Chemical Geology* **442**, 121–129.

Zhu, Z., Pranolo, Y., & Cheng, C.Y. (2015) Separation of uranium and thorium from rare earths for rare earth production – A review. *Minerals Engineering* **77**, 185–196.

Ziemann, M.A., Förster, H.-J., Harlov, D.E., & Frei, D. (2005) Origin of fluorapatite–monazite assemblages in a metamorphosed, sillimanite-bearing pegmatoid, Reinbolt Hills, East Antarctica. *European Journal of Mineralogy* **17**, 567–580.

Zozulya, D.R., Lyalina, L.M., & Savchenko, Y.E. (2017) Britholite-group minerals as sensitive indicators of changing fluid composition during pegmatite formation: evidence from the Keivy alkaline province, Kola peninsula, NW Russia. *Mineralogy and Petrology* **111**, 511–522.

Received June 6, 2017. Revised manuscript accepted March 8, 2018.